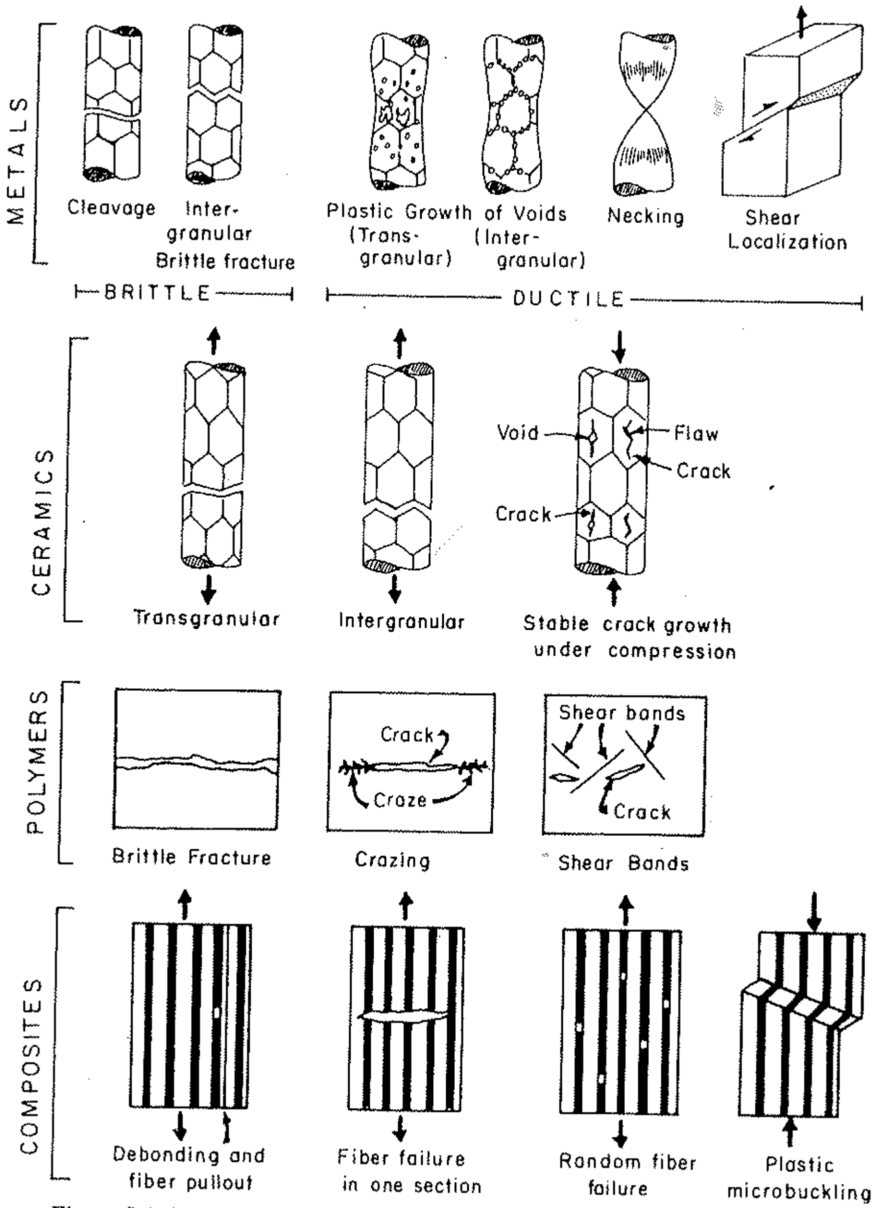

Figure 8.1 Schematic classification of fracture morphologies and processes. (After M. F. Ashby)

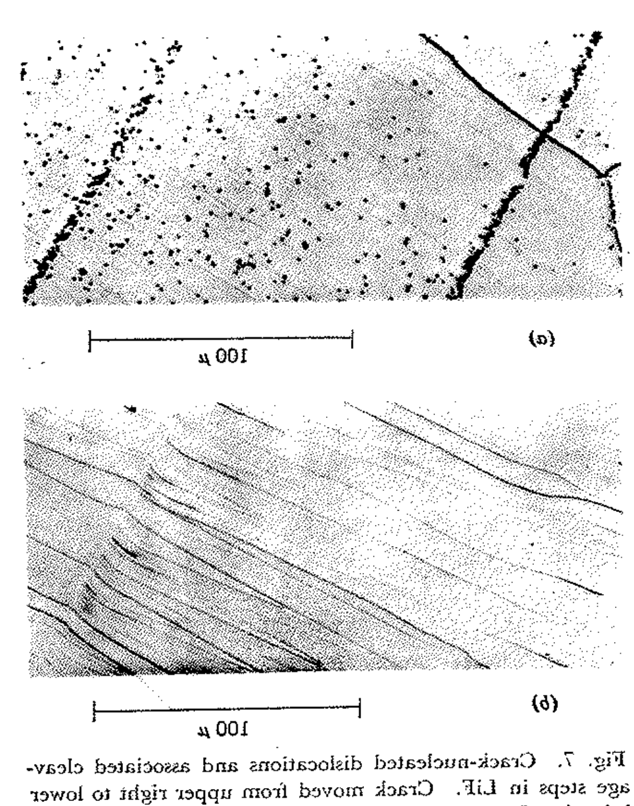

Fig. 7. Crack-nucleated dislocations and associated cleavage steps in LiF. Crack moved from upper right to lower left. (a) One cleavage surface of cracked crystal etch-pitted to reveal dislocations. (b) Matching cleavage surface, as cleaved. (Courtesy J. J. Gilman.[7])

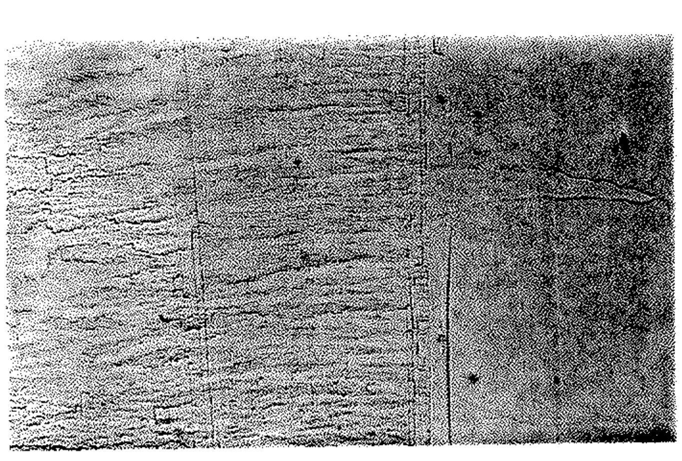

Fig. 8. Change in density of cleavage steps with change in temperature of cleavage. Zinc single crystal partially cleaved at 78°K, cleavage continued at 300°K. 78°K cleavage on left, 300°K cleavage on right.

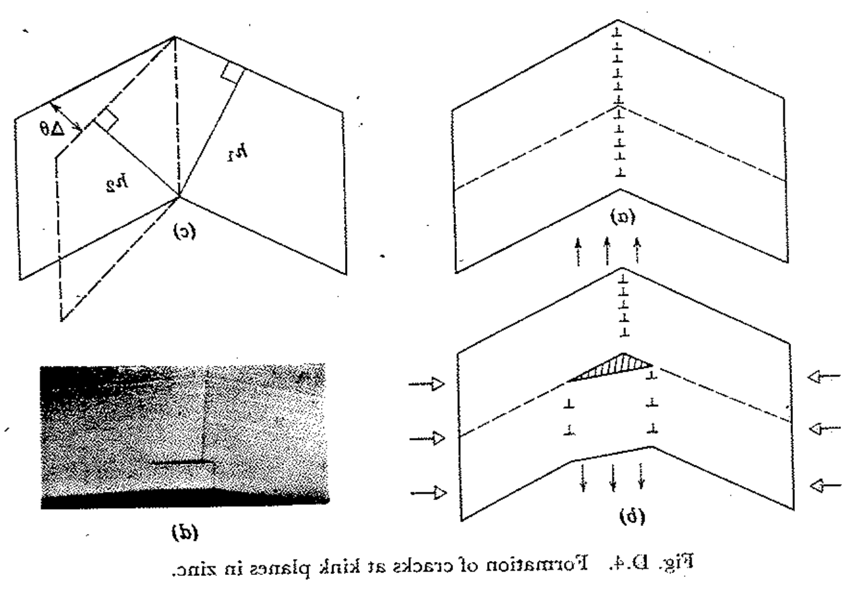

Fig. D.4. Formation of cracks at kink planes in zinc.

10 μ

…e of heavily deformed grain between two
Polycrystalline iron deformed 7.5% in

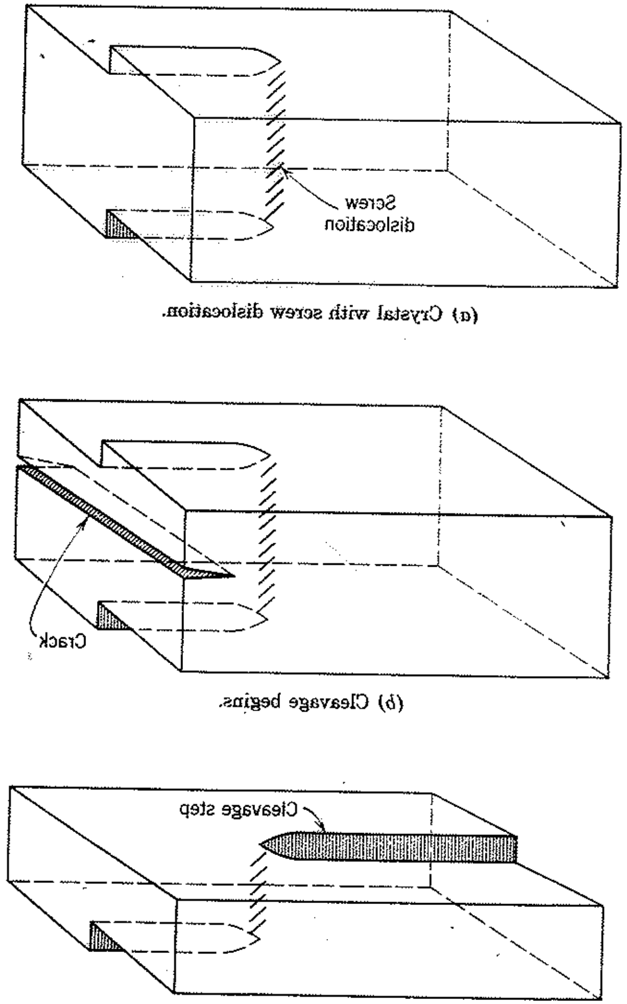

(a) Crystal with screw dislocation.

(b) Cleavage begins.

(c) After cleavage.

Fig. 4. Creation of cleavage step by screw dislocations.

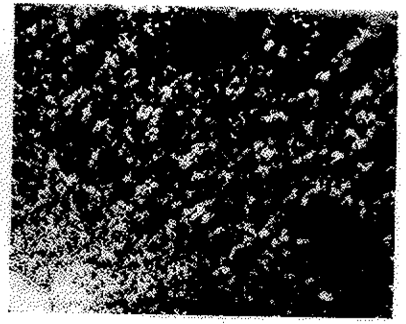

1 mm

Fig. 3. Fracture surface of tensile specimen of polymethyl methacrylate. Molecular weight = 90,000.

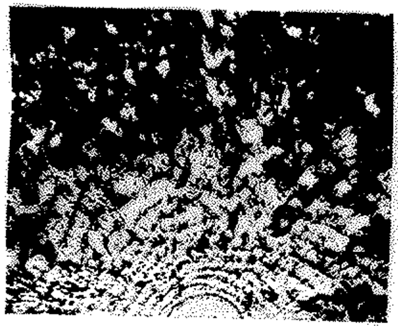

1 mm

Fig. 4. Fracture surface of tensile specimen of polymethyl methacrylate. Molecular weight = 120,000.

1 mm

Fig. 5. Fracture surface of tensile specimen of polymethyl methacrylate. Molecular weight = 200,000.

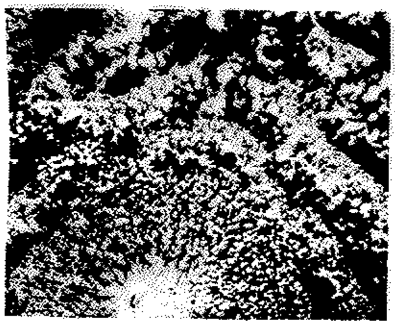

1 mm

Fig. 6. Fracture surface of tensile specimen of polymethyl methacrylate. Molecular weight = 490,000.

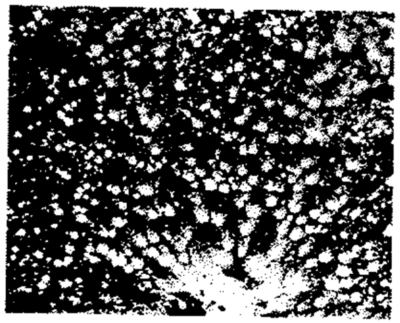

1 mm

Fig. 7. Fracture surface of tensile specimen of polymethyl methacrylate. Molecular weight = 3,160,000.

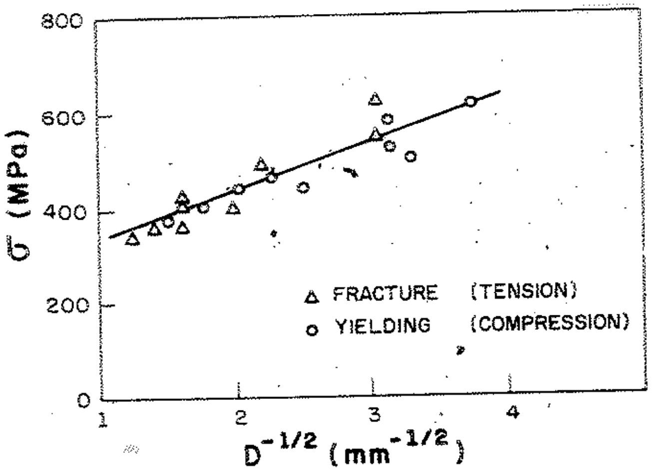

Figure 8.21 Effect of grain size on fracture and yield stress of a carbon steel at 77 K. (Adapted from J. R. Low, in *Madrid Colloquium on Deformation and Flow of Solids* (Berlin: Springer-Verlag, 1956), p. 60)

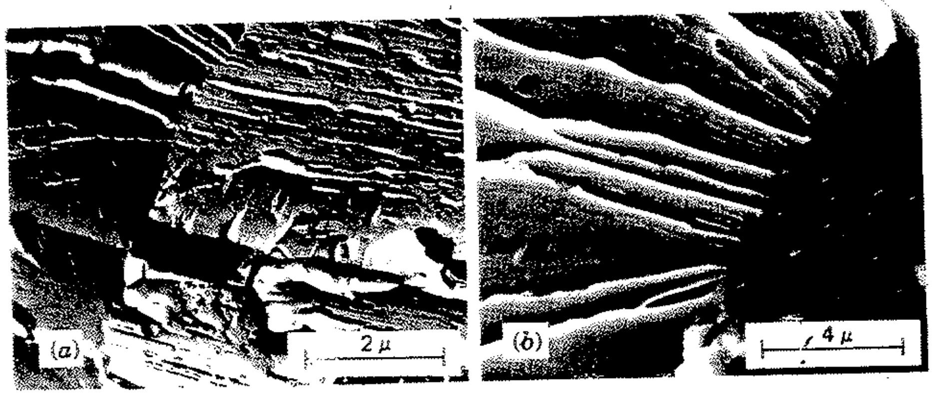

FIGURE 7.27 Cleavage fracture in a low-carbon steel. Note parallel plateau and ledge morphology and river patterns reflecting crack propagation along many parallel cleavage planes: (*a*) TEM; (*b*) SEM.

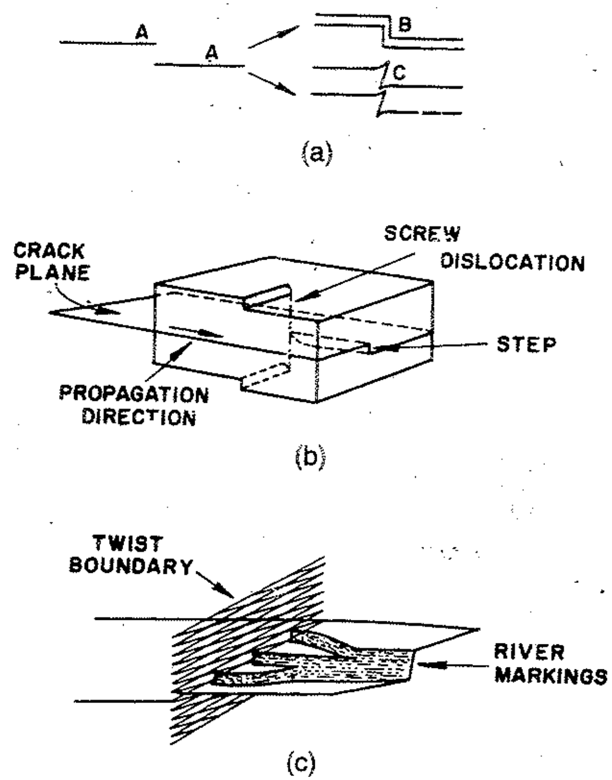

Figure 8.23 Formation of cleavage steps. (a) Parallel cracks (*A*, *A*) join together by cleavage (*B*) or shear (*C*). (b) Cleavage step initiation by the passage of a screw dislocation. (c) Formation of river markings after the passage of a grain boundary. (Adapted from D. Broek, *Elementary Engineering Fracture Mechanics*, 3d ed. (The Hague, Netherlands: Martinus Nijhoff, 1982), p. 33)

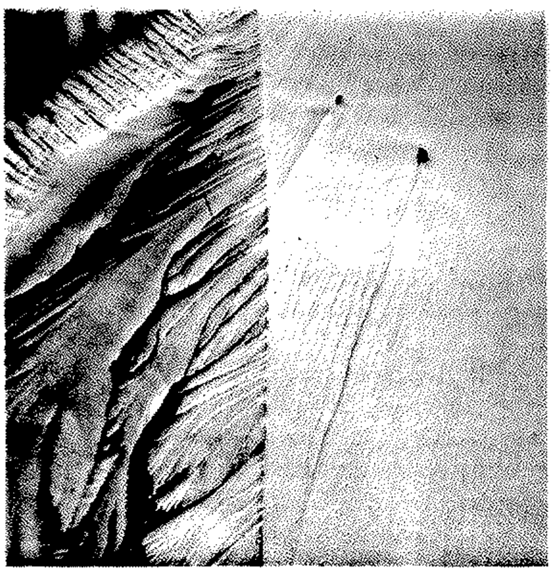

100 μ

Fig. 3. Increase in cleavage step density for crack crossing 3° twist boundary in 3% Si-Fe crystal cleaved at 78°K. Direction of crack propagation was from upper right to lower left.

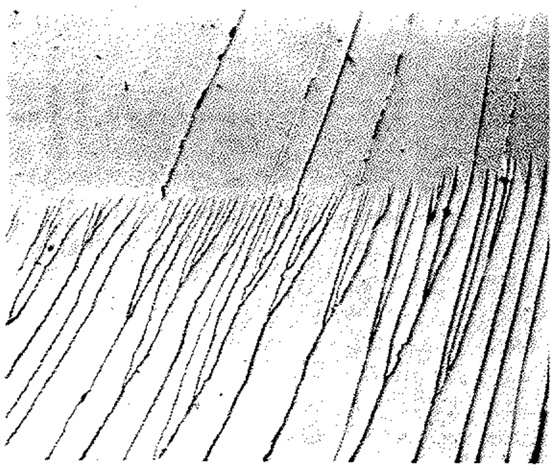

100 μ

Fig. 4. Creation of cleavage steps at tilt-twist boundary in LiF. Crack moved from top to bottom. Boundary: approximately 0.85° twist, 0.87° tilt. (Courtesy J. J. Gilman.[7])

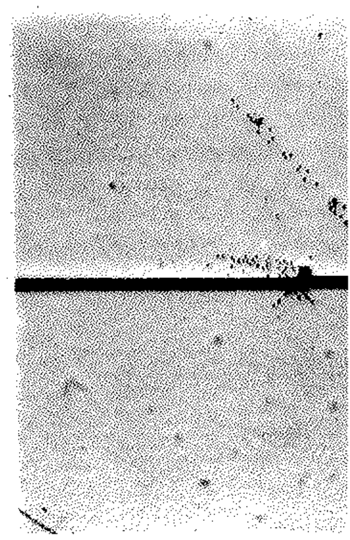

100

Fig. 5. Etch-pit pattern showing dislocatic
Crack tip rounded and crack widened by pc
J. J. Gilman.[9])

1(

Fig. 6. Cleavage steps originating at poin
started immediately at 78°K in 3% Si-Fe c
to lower left.

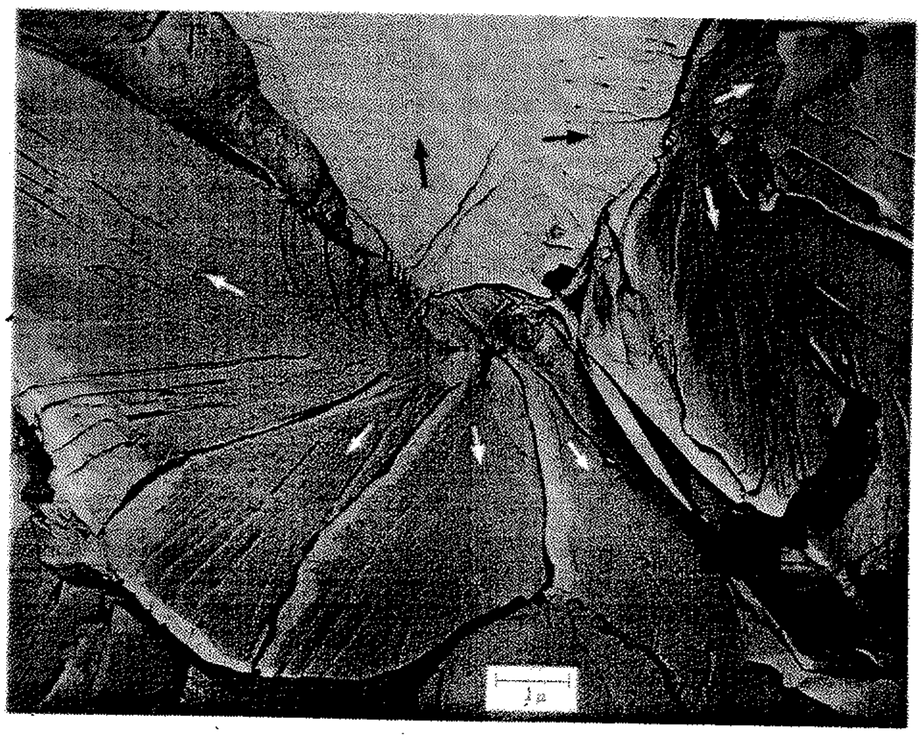

Fig. 17.23. River markings on the cleavage surface of polycrystalline iron fractured at 77°K. (Low, 1959. Courtesy of M.I.T. Press.)

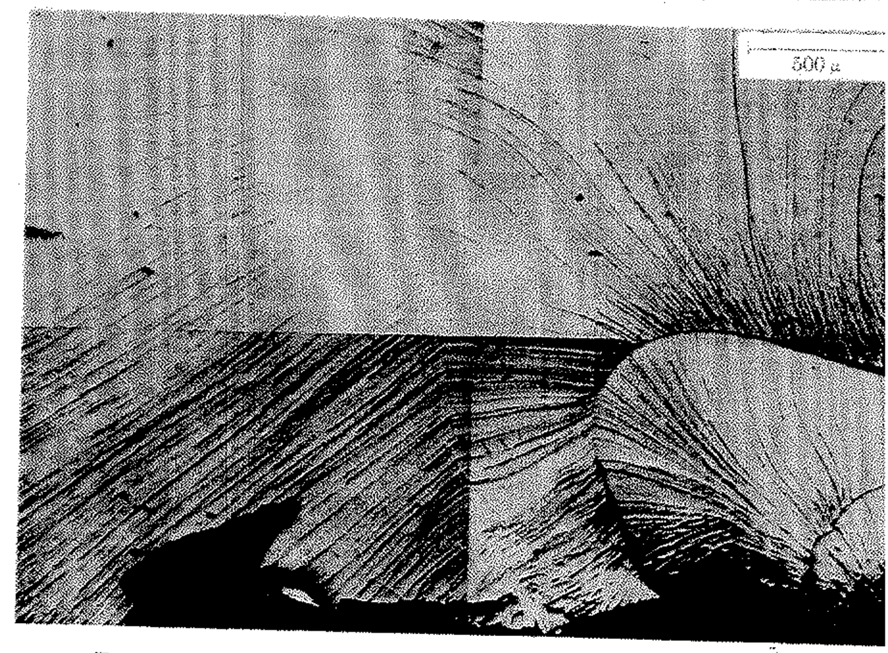

Fig. 17.24. Cleavage steps on a cube plane of a KCl crystal at 400°C.

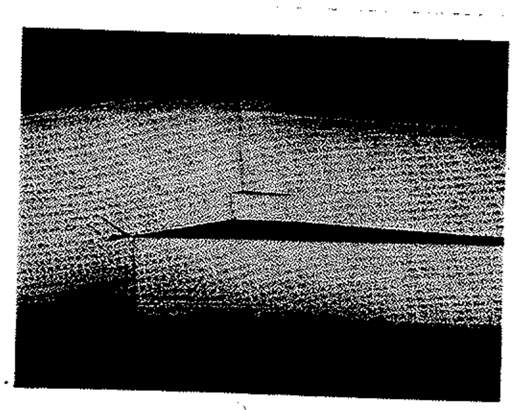

Fig. 17.10. Cleavage fractures in a single crystal of zinc, approximately ten times magnified. (Gilman, 1954. Courtesy of Am. Inst. Mining and Metallurgical Engineers.)

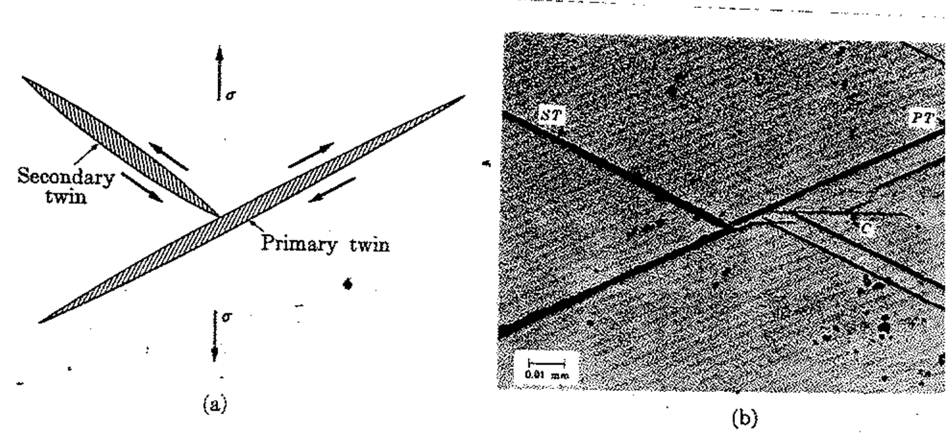

Fig. 17.11. (a) Crack nucleation by the intersection of two deformation twins. (b) effect as observed in silicon iron: PT, primary twin; ST, secondary twin; C, crack emanating from intersection. (Hull, 1960. Courtesy of Pergamon Press.)

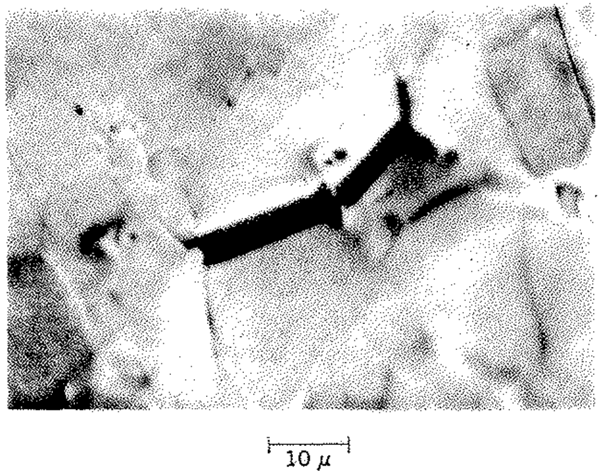

Fig. 11. Example of distorted region at grain boundary between cleaved grains in polycrystalline iron deformed 7.5% in bending at 78°K.

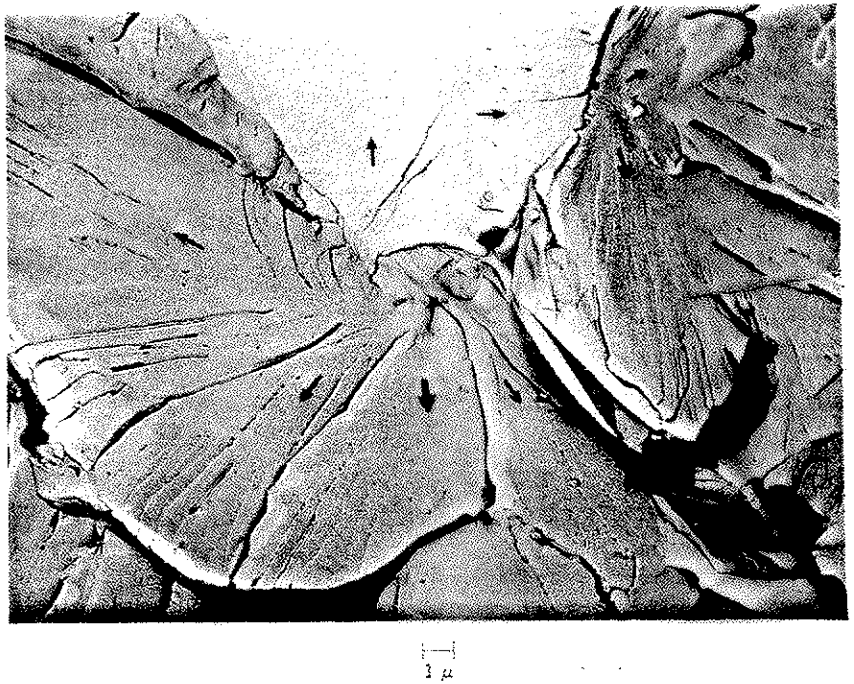

Fig. 12. Example of cleavage step pattern radiating from a point in polycrystalline iron fractured at 78°K. Arrows indicate direction of crack propagation as deduced from river patterns. Electron micrograph.

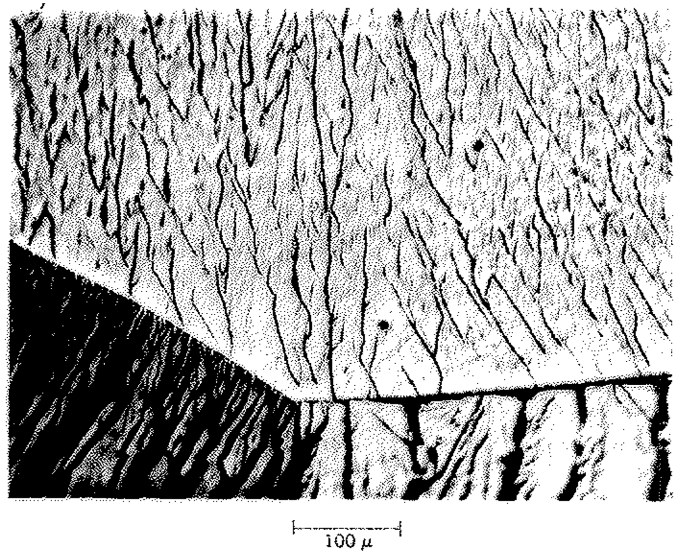

Fig. 9. Cleavage steps originating at two high-angle boundaries. Left boundary approximately 10° tilt; right boundary approximately 10° tilt plus 3° twist. Note radiating pattern between large cleavage steps right boundary. 3% Si-Fe cleaved at 78°K, direction of crack propagation top to bottom.

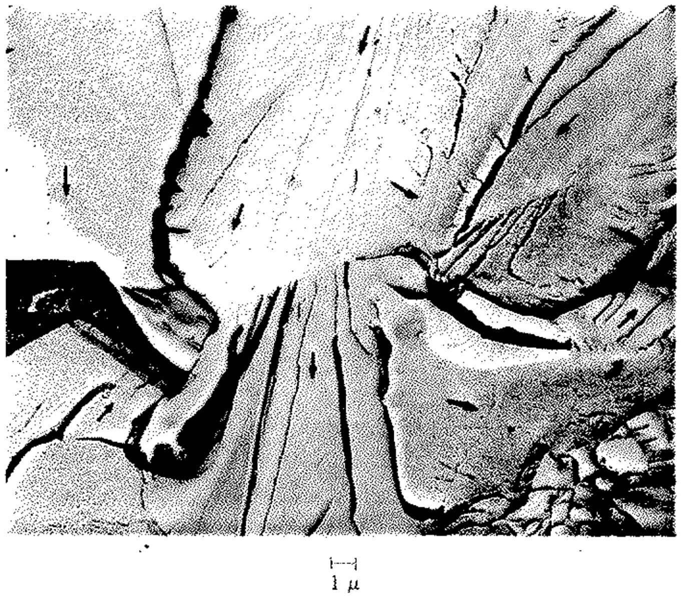

Fig. 10. Cleavage pattern of polycrystalline iron at 78°K. Approximately 0.02-mm grain size; broken in tension; reduction in area to fracture 26.5%. Note variability of direction of propagation of crack from grain to grain and dark irregular bands at some grain boundaries (see Fig. 11). Electron micrograph.

Fig. 1. Cleavage step "river pattern." 3% Si-Fe single-crystal cleavage surface. Cleaved at 78°K. Direction of crack propagation is from top to bottom of the photograph. Note low-angle tilt boundary.

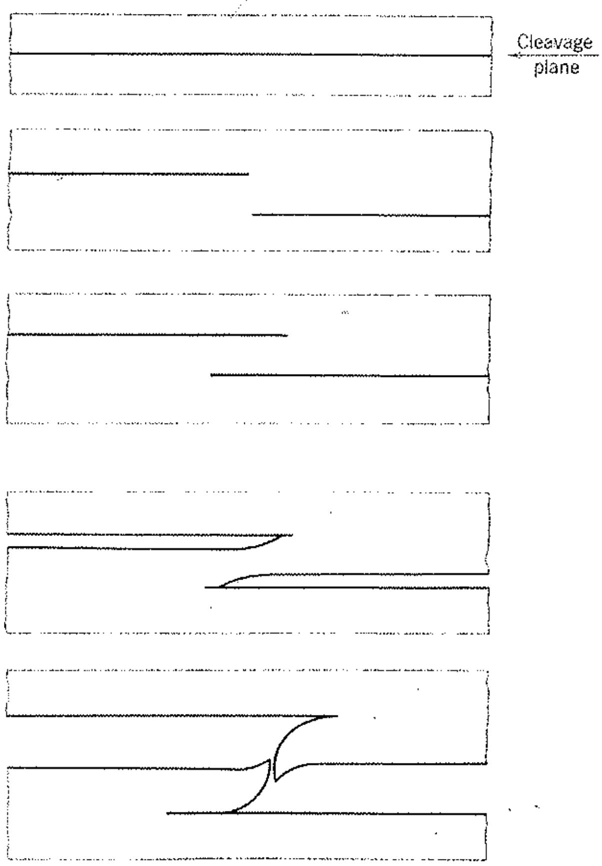

Fig. 2. Schematic representation of cleavage step formation between two parallel cleavage cracks on differing crystal planes. Ductile fracture shown is one mode of parting to form steps; for others, see Gilman[2] and Berry.[3]

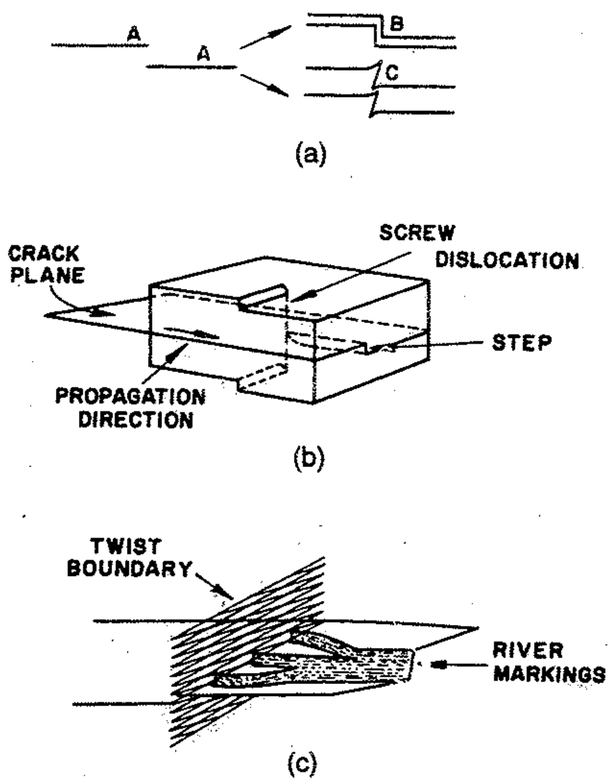

Figure 8.23 Formation of cleavage steps. (a) Parallel cracks (A, A) join together by cleavage (B) or shear (C). (b) Cleavage step initiation by the passage of a screw dislocation. (c) Formation of river markings after the passage of a grain boundary. (Adapted from D. Broek, *Elementary Engineering Fracture Mechanics,* 3d ed. (The Hague, Netherlands: Martinus Nijhoff, 1982), p. 33)

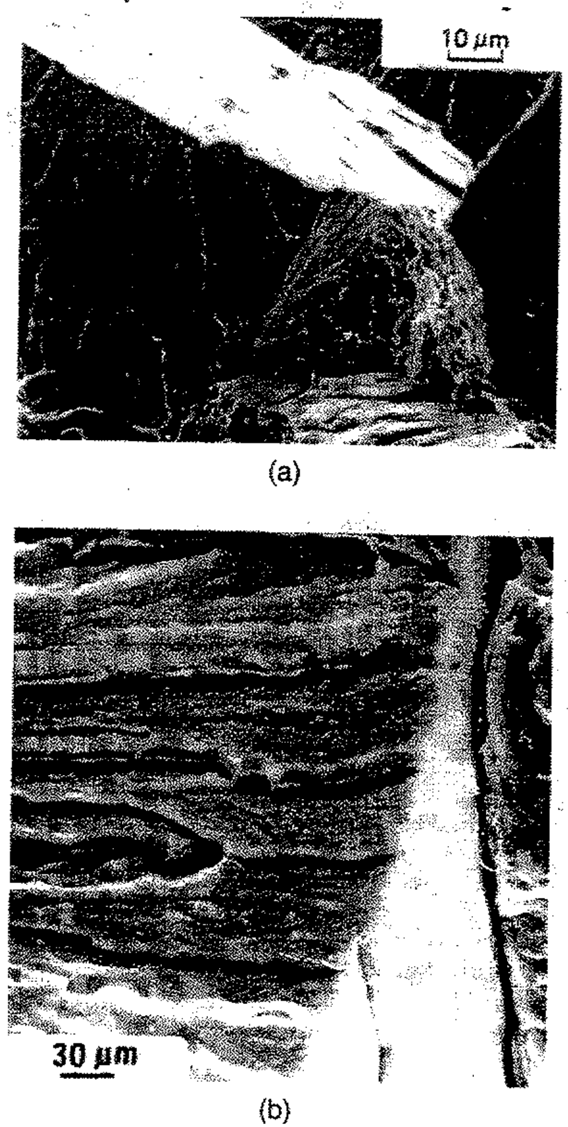

Figure 8.22 (a) Cleavage facets in 300-M steel (scanning electron micrograph). (b) River markings on a cleavage facet in 300-M steel (scanning electron micrograph).

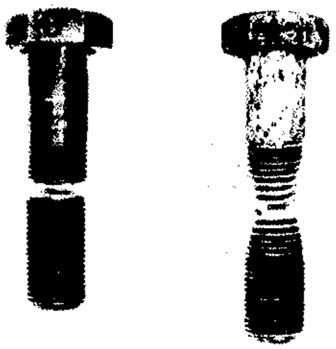

Fig. 17·1 Two bolts intentionally pulled to failure in tension to demonstrate brittle and ductile behavior. The brittle bolt, left, was hard, Rockwell C 57; the ductile bolt was soft, Rockwell C 15. (Courtesy of D. J. Wulpi, International Harvester Company.)

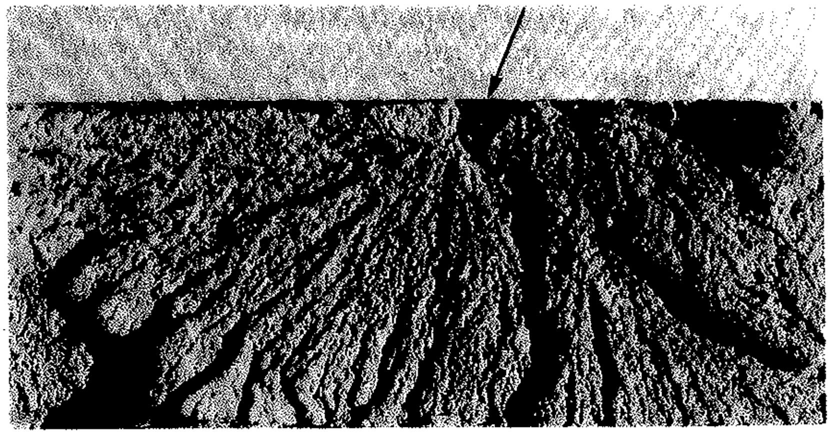

ig. 17·2 "Chevron" pattern points to the origin of the rittle fracture (arrow) in this specimen. A fatigue fracture s also apparent in the upper right-hand corner. (Courtesy f D. J. Wulpi, International Harvester Company.)

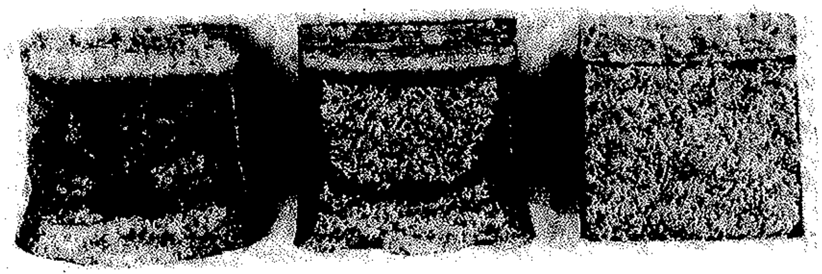

Fig. 17·3 Combinations of fracture modes are shown by fracture surfaces of three impact test specimens which were broken at different temperatures. On the left, fracture is mostly shear; in the center, combined shear and cleavage; and on the right, cleavage. (Courtesy of D. J. Wulpi, International Harvester Company.)

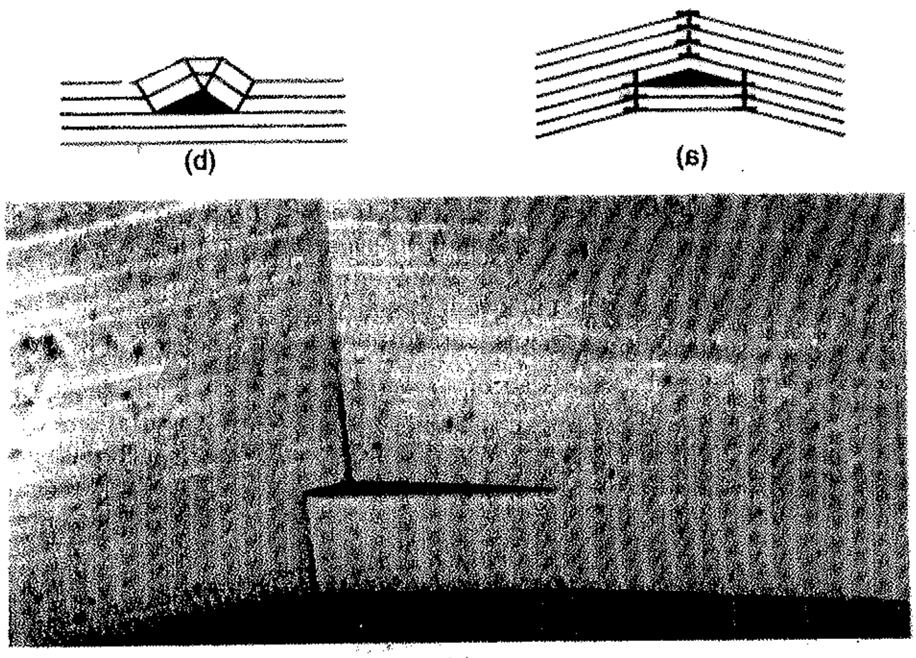

Figure 8.5 Crack nucleation by (a) lattice rotation due to bend planes and (b) deformation twins. (c) Crack nucleation in zinc due to lattice rotation associated with bend planes. (Reprinted with permission from [J. J. Gilman, *Physical Nature of Plastic Flow and Fracture*, General Electric Report No. 60-RL-2410M, April, 1960.], p. 83.)

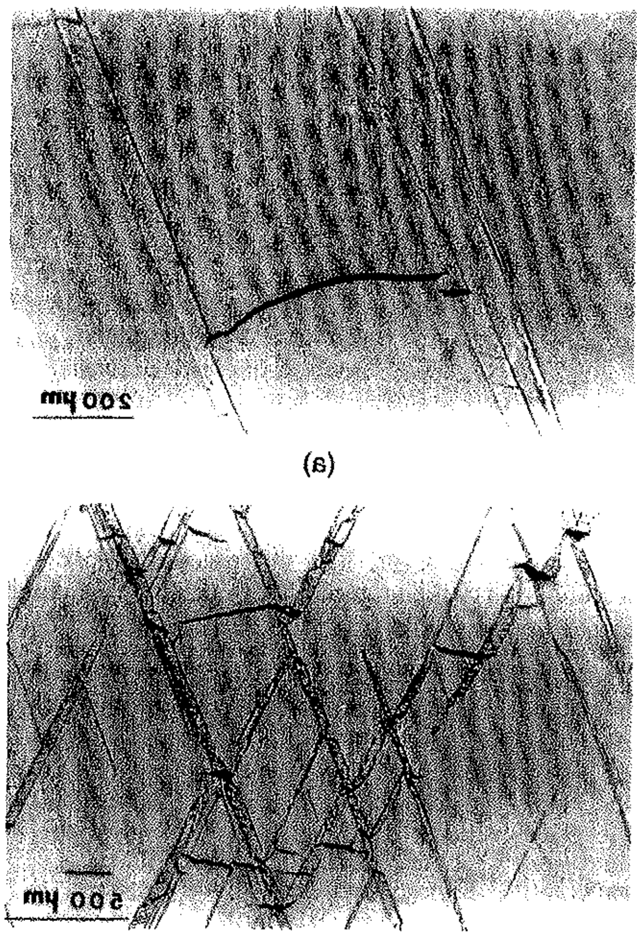

Figure 8.6 Initiation of failure by microcrack formation in tungsten deformed at approximately $10^4\ s^{-1}$ at room temperature. (a) Twin steps. (b) Twin steps and twin–twin intersection. (From T. Dümmer, J. C. LaSalvia, M. A. Meyers, and G. Ravichandran, *Acta Mat.*, (1998))

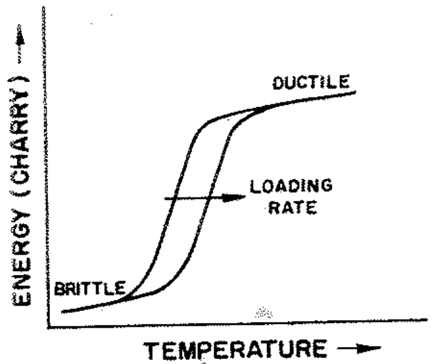

Figure 8.19 Ductile–brittle transition in steel and the effect of loading rate (schematic).

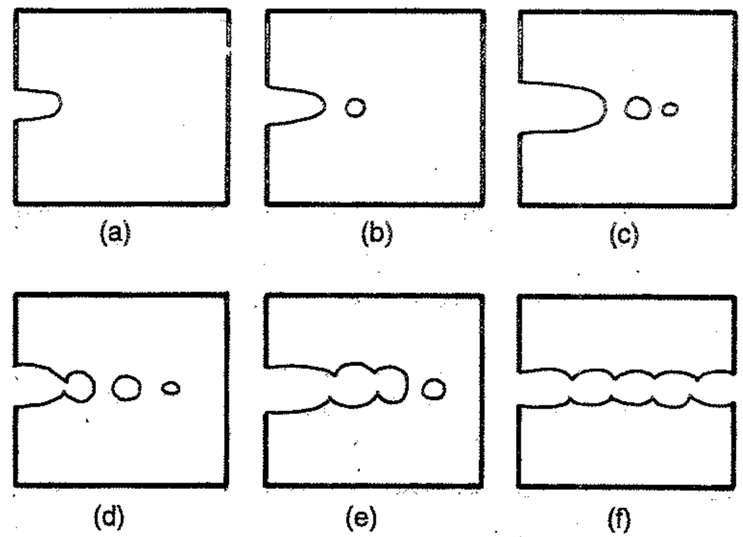

Figure 8.15 Sequence of events in the propagation of ductile fracture by nucleation, growth, and coalescence of voids.

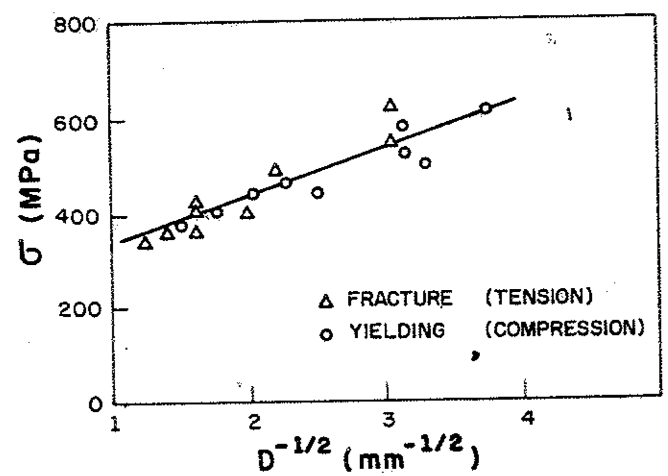

Figure 8.21 Effect of grain size on fracture and yield stress of a carbon steel at 77 K. (Adapted from J. R. Low, in *Madrid Colloquium on Deformation and Flow of Solids* (Berlin: Springer-Verlag, 1956), p. 60)

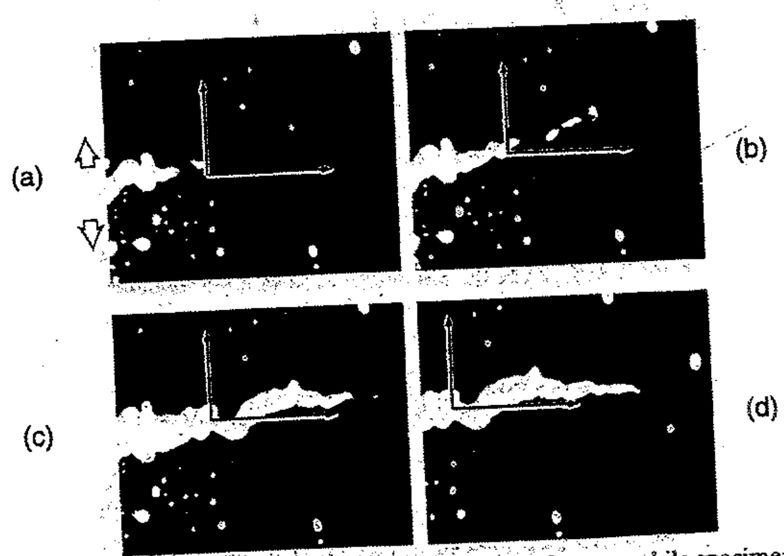

Figure 8.16 Observation of progression of ductile fracture while specimen is stressed in high-voltage transmission electron microscope. Referential is fixed to material (Courtesy of L. E. Murr).

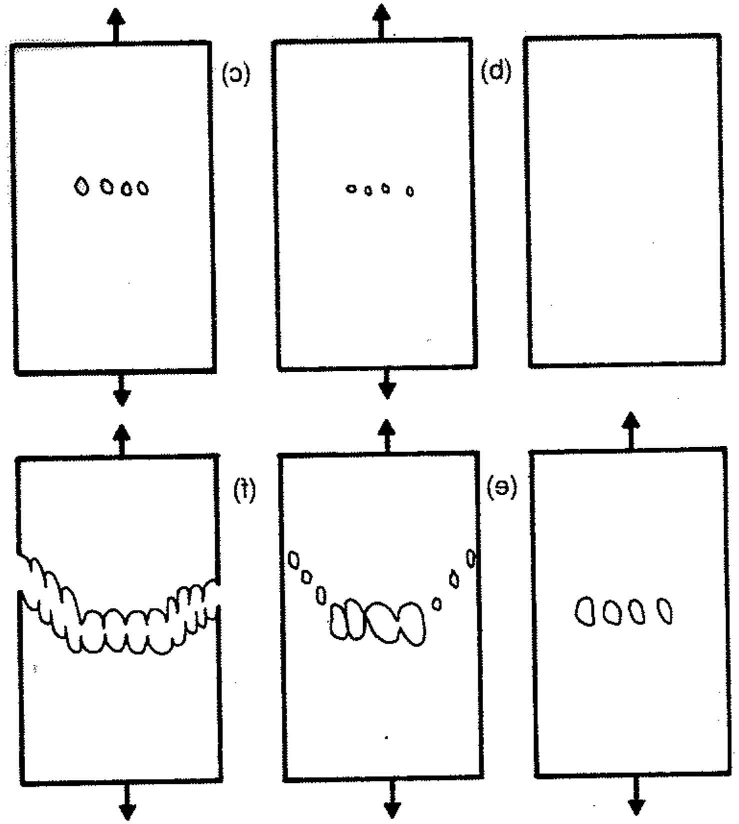

Figure 8.14 Schematic sequence of events leading to the formation of a cup-and-cone fracture.

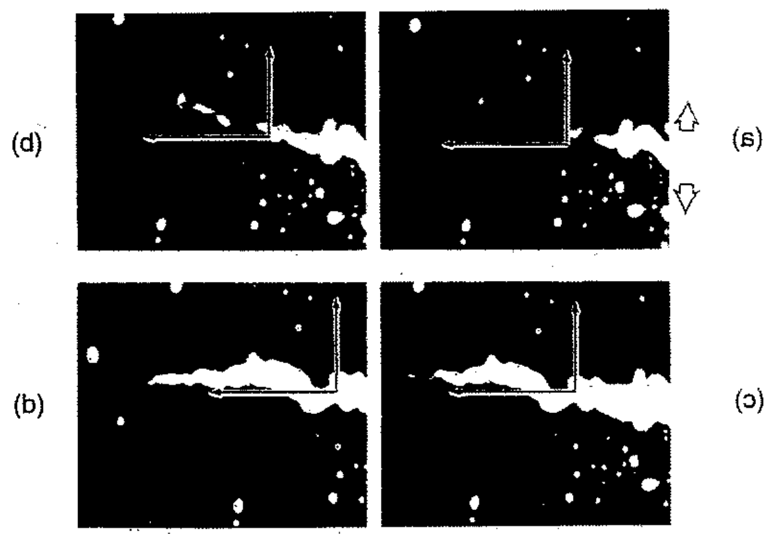

Figure 8.16 Observation of progression of ductile fracture while specimen is stressed in high-voltage transmission electron microscope. Referential is

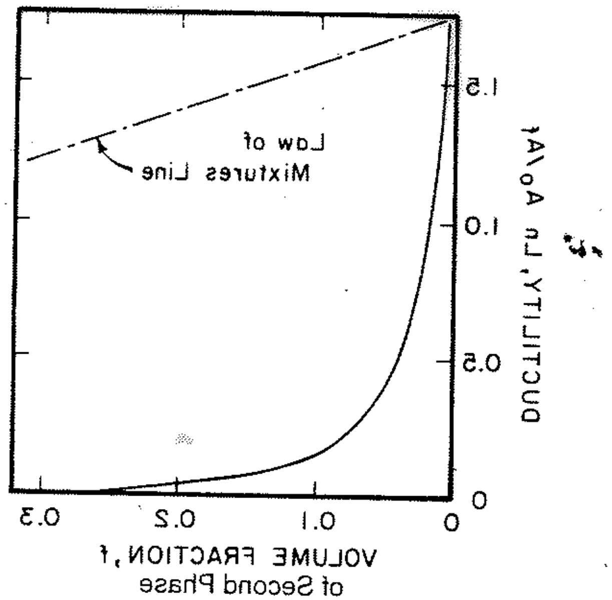

Figure 8.17 Combined plot of ductility vs. volume fraction of second phase, *f*, for copper specimens containing various second phases and for notched copper specimens. The dashed line represents the prediction from the law of mixtures, assuming zero ductility for the second-phase particles. (From B. I. Edelson and W. J. Baldwin, Jr., *Trans. ASM*, 55, p. 230 (1962))

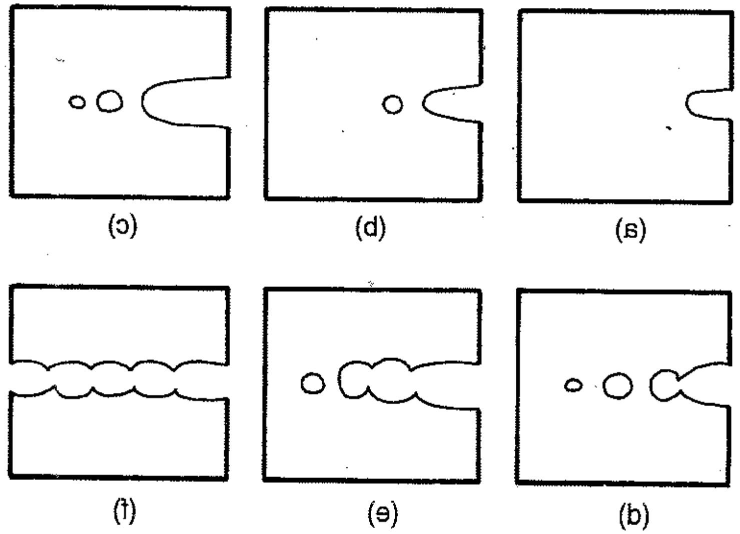

Figure 8.15 Sequence of events in the propagation of ductile fracture by nucleation, growth, and coalescence of voids.

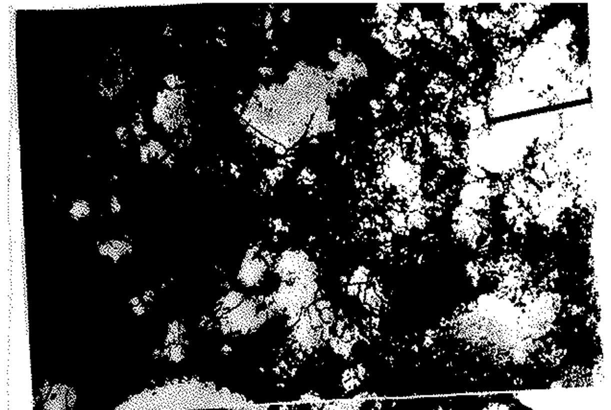

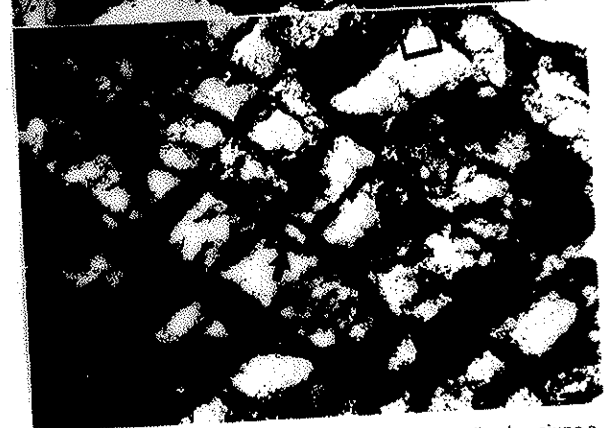

1 Longitudinal section of 10% rolled specimen: 1 μm marker is along rolling direction (RD)

a equiaxed cells; b HWD structure – arrow indicates initial stages of formation of first generation microband

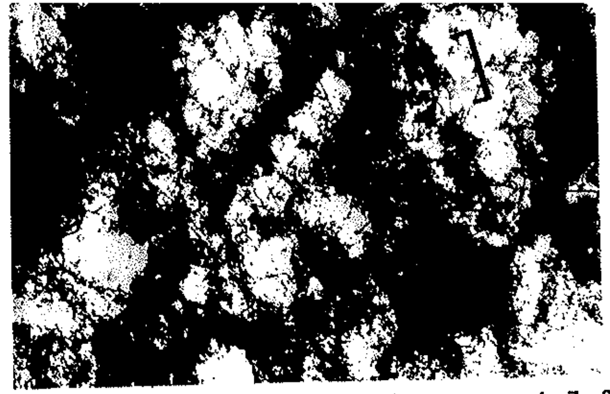

3 Early stages of DDW formation (arrowed) in specimen rolled 5% (longitudinal section, 1 μm marker is along RD)

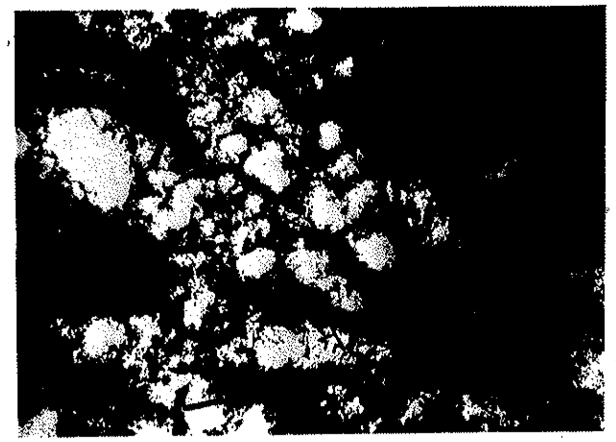

Well developed dislocation walls (arrowed) in specimen rolled 10% (longitudinal section, 1 μm marker is along RD)

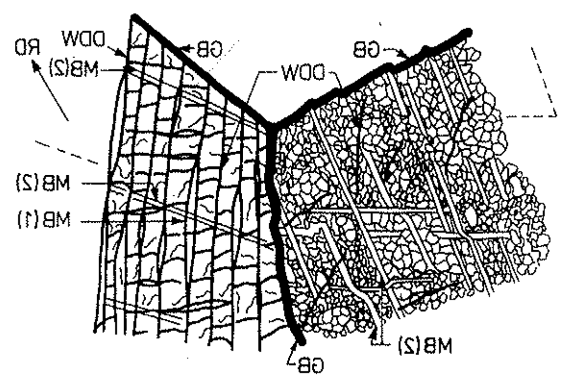

broken lines show {111} trace directions; RD rolling direction; GB grain boundaries

10 Idealised fully developed microstructure in copper at low to medium strains, consisting of equiaxed cells, dense dislocation walls (DDW), and first (MB(1)) and second (MB(2)) generation microbands: intersecting DDWs form HWD structures in approximately 30% of grains

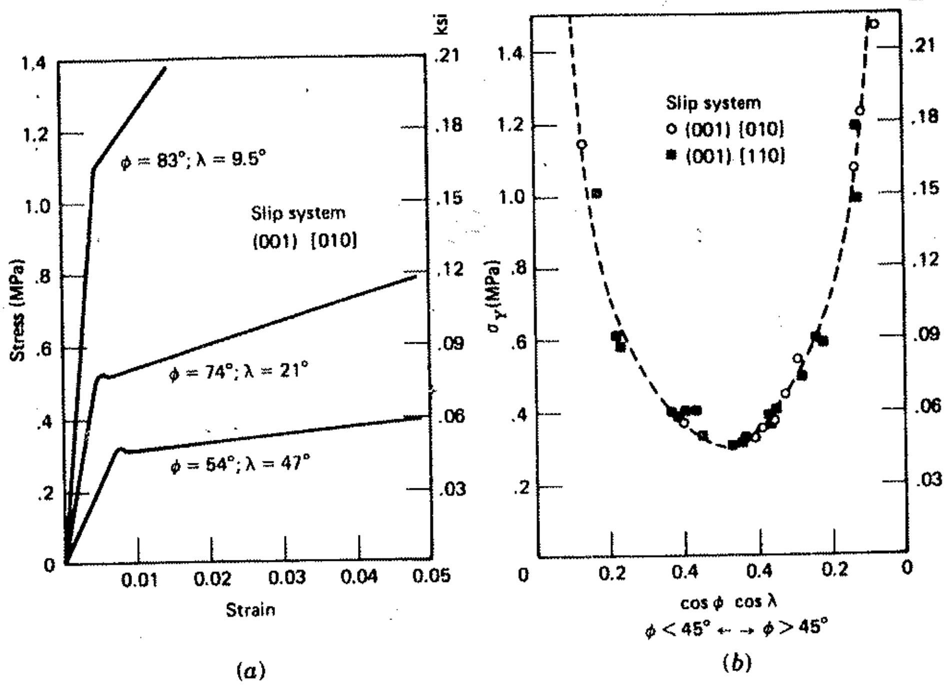

FIGURE 3.4 Yield behavior of anthracene single crystals. (*a*) Axial stress–strain curves for crystals possessing different orientations relative to the loading axis; (*b*) axial stress for many crystals plotted versus respective Schmid factors. Dotted curve represents relation given by Eq. 3-3 where τ_{crss} = 137 kPa. (After Robinson and Scott;[11] reprinted with permission from Robinson, *Acta Met.* 15 (1967), Pergamon Press, Elmsford, NY.)

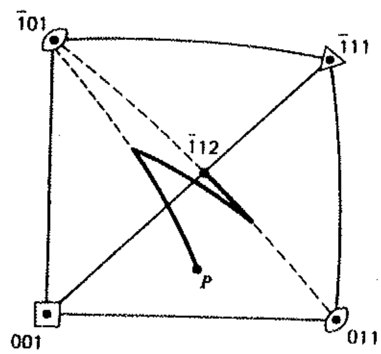

FIGURE 3.9 Lattice rotation of FCC crystal involving "overshoot" of primary and conjugate slip systems.

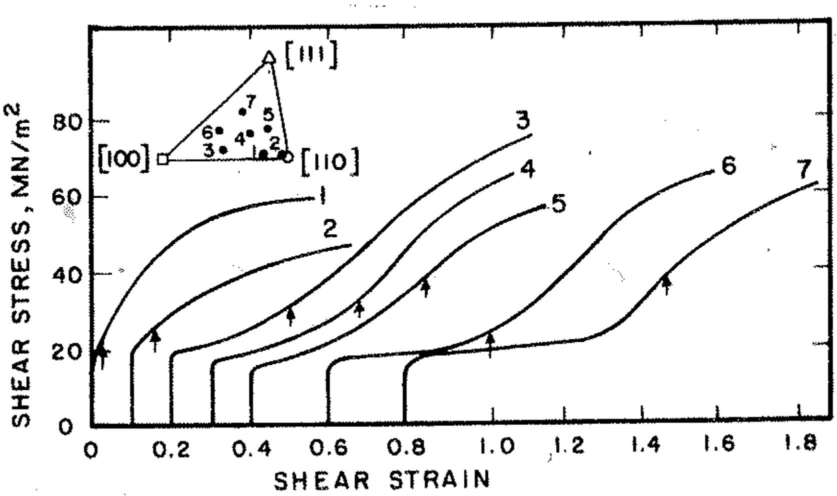

Figure 6.12 Shear-stress vs. shear-strain curves for Nb(BCC) monocrystals at different crystallographic orientations; arrows indicate calculated strain at which conjugate slip is initiated. (From T. E. Mitchell, *Prog. App. Matls. Res.* 6 (1964) 117)

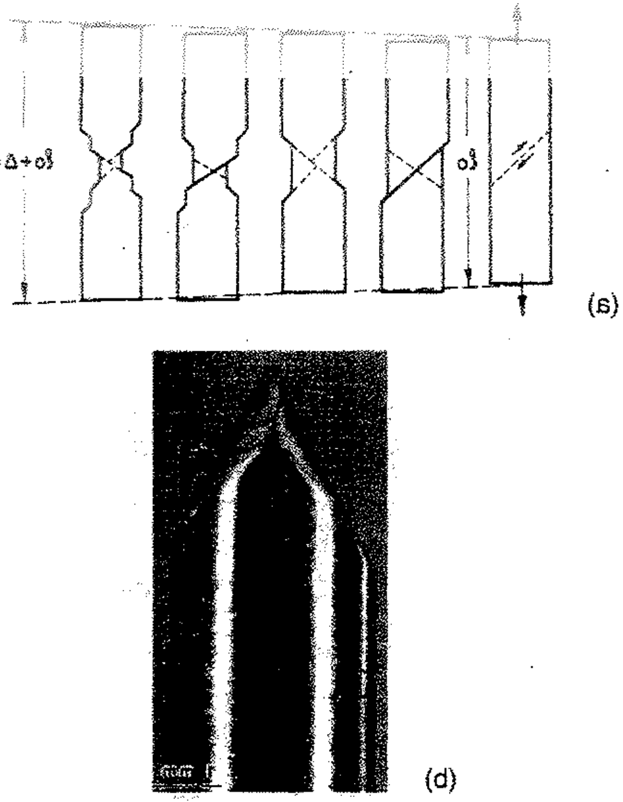

Figure 8.2 (a) Failure by shear (glide) in a pure metal. (Reprinted with permission from D. Broek, *Elementary Engineering Fracture Mechanics*, 3d ed. The Hague, Netherlands: Martinus Nijhoff, (1982), p. 33.) (b) A point fracture in a soft single-crystal sample of copper. (Courtesy of J. D. Embury)

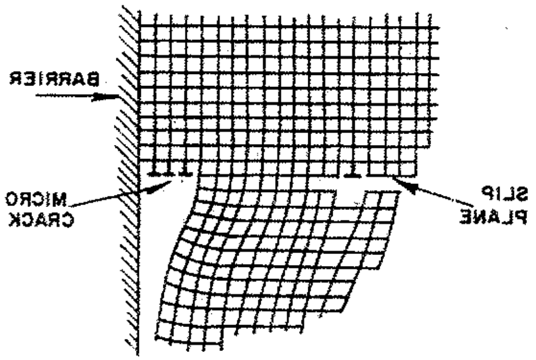

Figure 8.3 Grouping of dislocations piled up at a barrier and leading to the formation of a microcrack (Zener–Stroh crack).

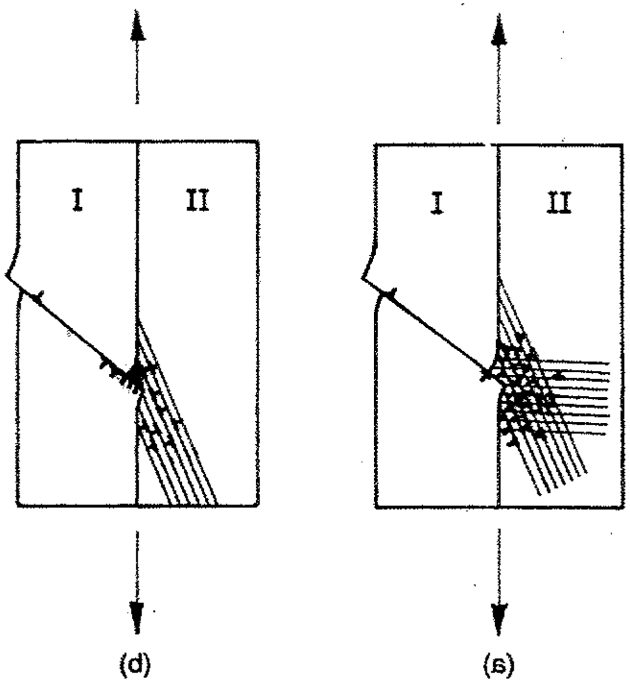

Figure 8.4 Bicrystal with a slip band in grain I. (a) The stress concentration at the boundary of the barrier due to slip band is fully relaxed by multiple slip. (b) The stress concentration is only partially relaxed, resulting in a crack at the boundary.

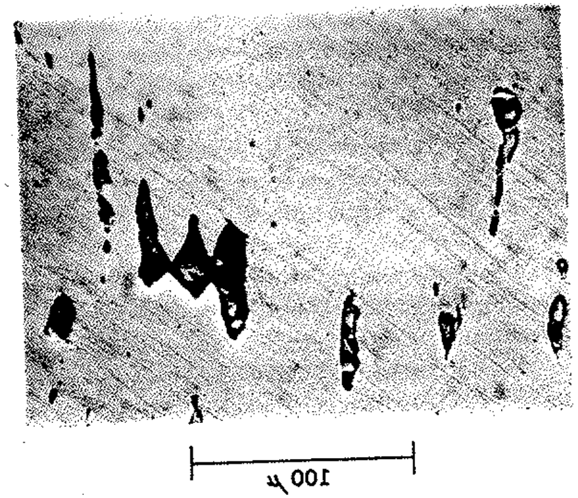

Fig. 3. Cavities coalescing in the neck of a tensile specimen of copper. (After Puttick.[51])

Fig. 4. Section through the neck of the tensile specimen from which Fig. 3 was taken. (After Puttick.[51])

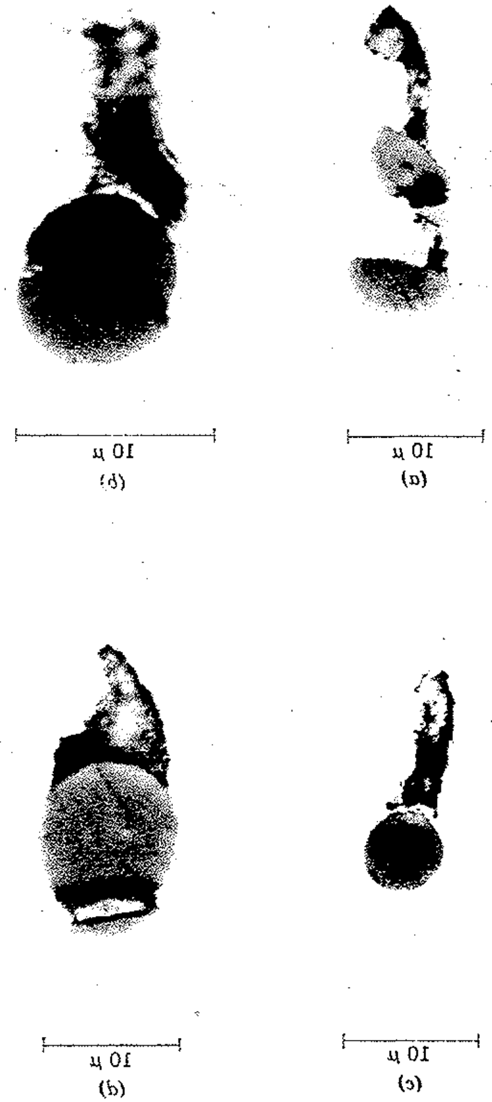

Fig. 5. Examples of cavities forming at oxide inclusions. (Tensile axis is vertical.) (After Puttick.[51])

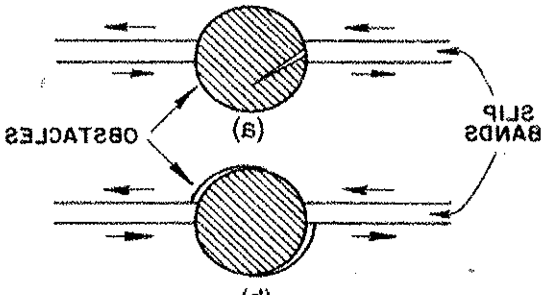

Figure 8.11 Nucleation of a cavity at a second-phase particle in a ductile material. (Adapted with permission from B. R. Lawn and T. R. Wilshaw, *Fracture of Brittle Solids* (Cambridge: Cambridge University Press, 1975), p. 40)

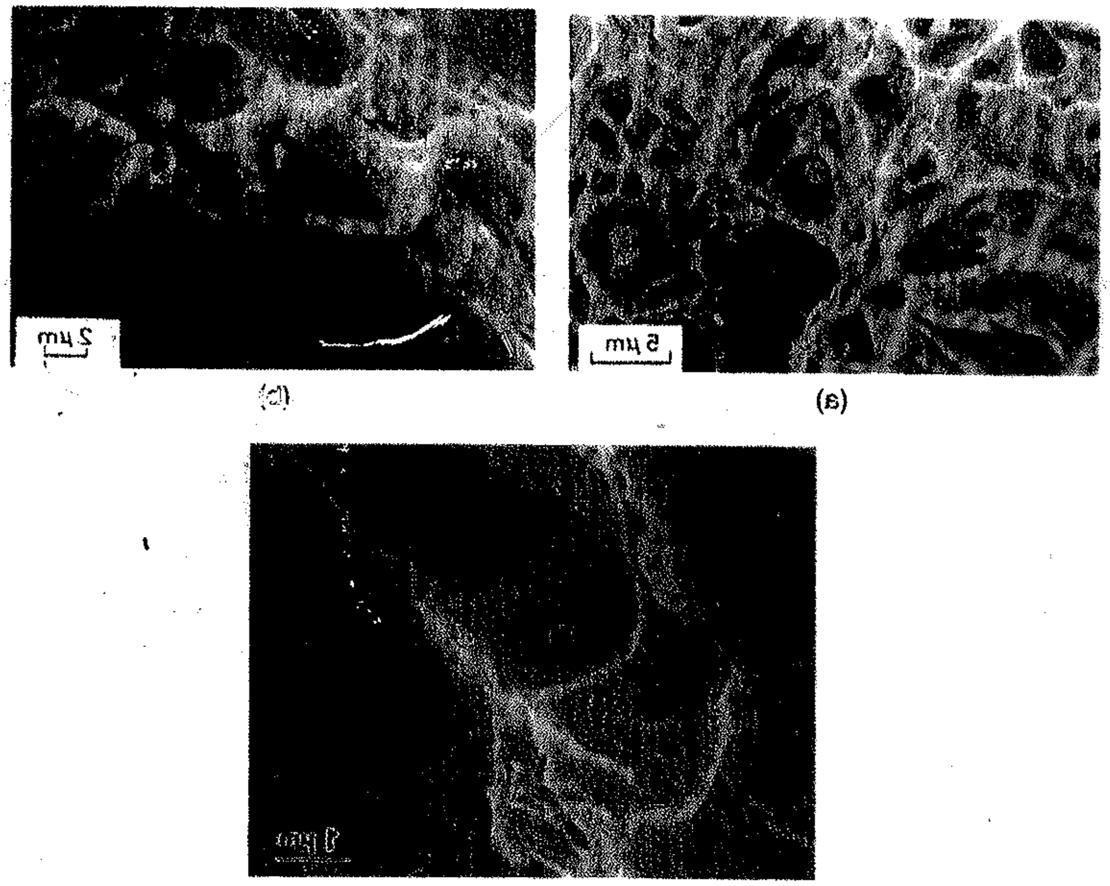

(a) (b) (c)

Figure 8.12 (a) Scanning electron micrograph of dimple fracture resulting from the nucleation, growth, and coalescence of microcavities. Note the inclusion particles, which served as the microcavity nucleation sites. (b) Fractured metal carbide particle (see the center of the picture) in Inconel 718 superalloy. (c) Inclusion in steel.

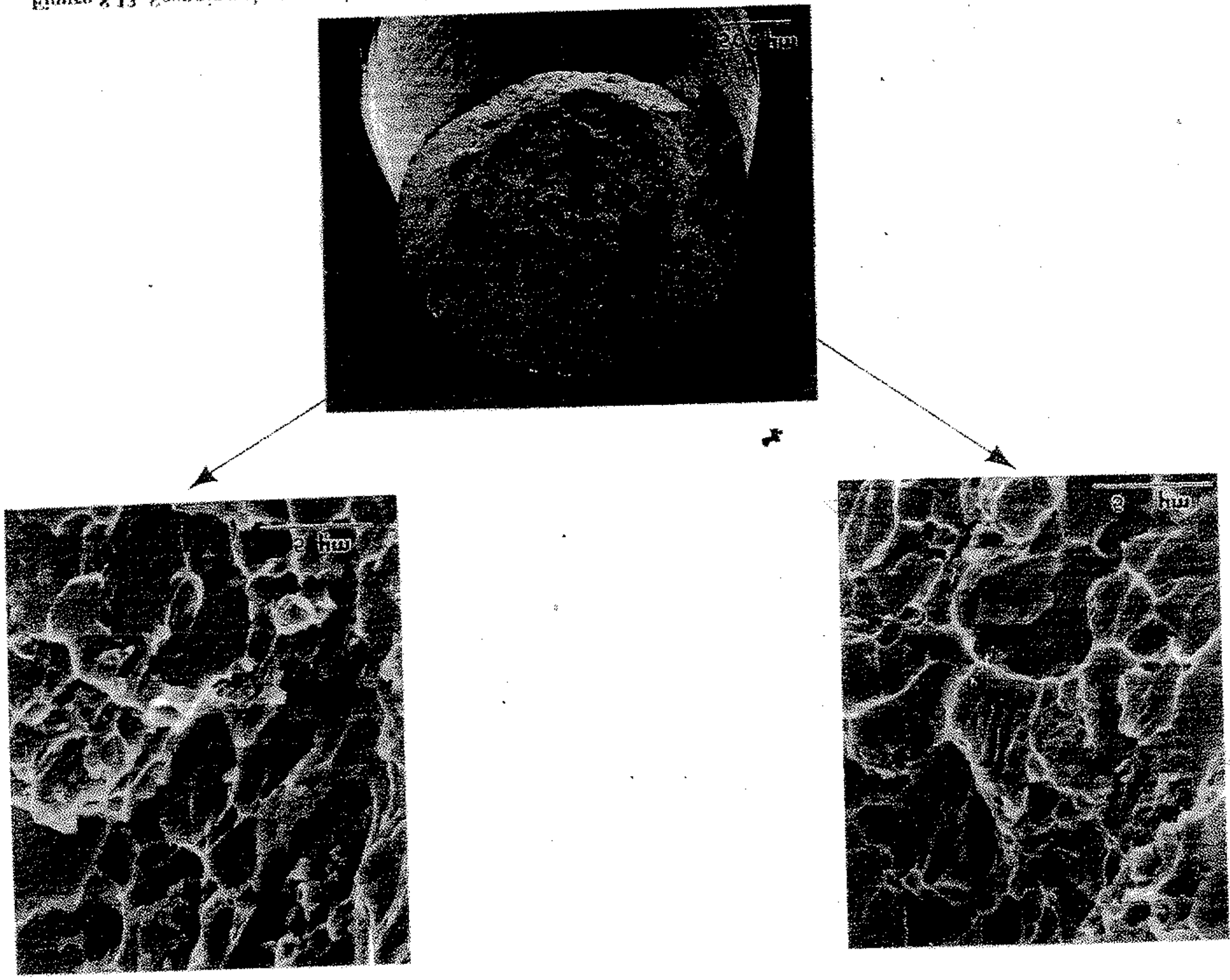

Figure 8.13 Scanning electron micrographs at low magnification (center) and high magnification (right and left) of AISI 1008 steel specimen ruptured in tension. Notice the equiaxal dimples in the central region and elongated dimples on the shear walls (the sides of the cup).

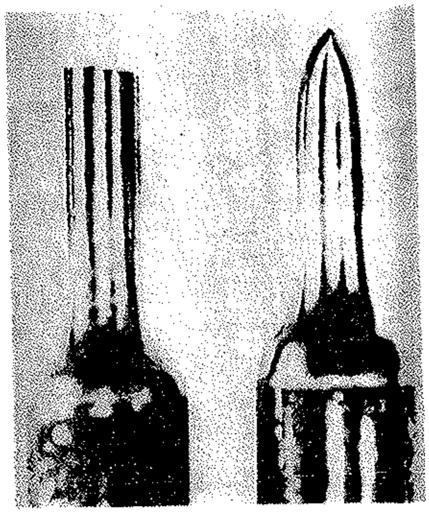

Fig. 2. Extremes of fracture behavior in iron crystals tested at −196°C. (*a*) Chisel edge fracture 100% reduction in area. (*b*) Cleavage fracture. (After Allen, Hopkins, and McLennan.[2])

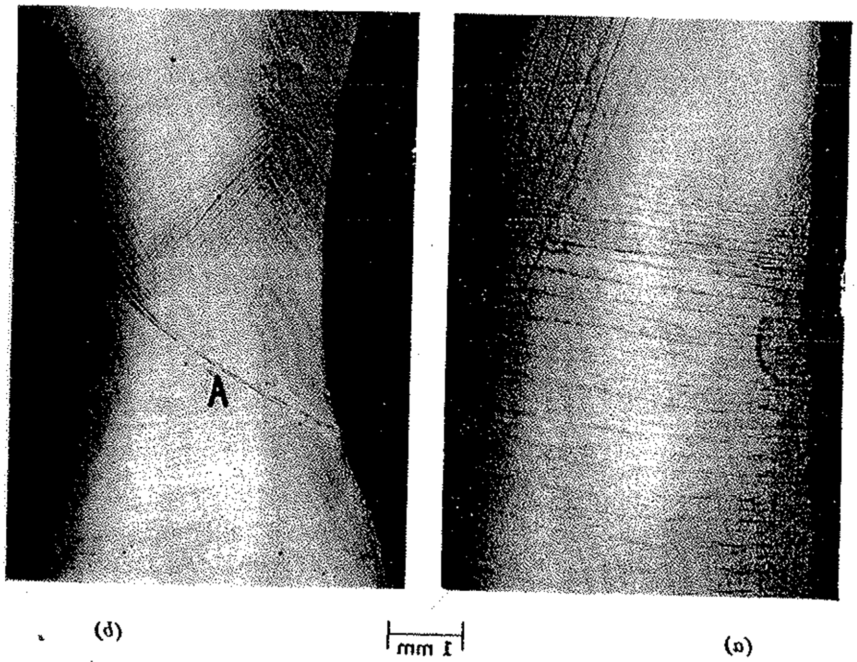

Fig. 4. Coarse slip bands in the necks of aluminum crystals. In (*b*), the final shear zone A is shown.

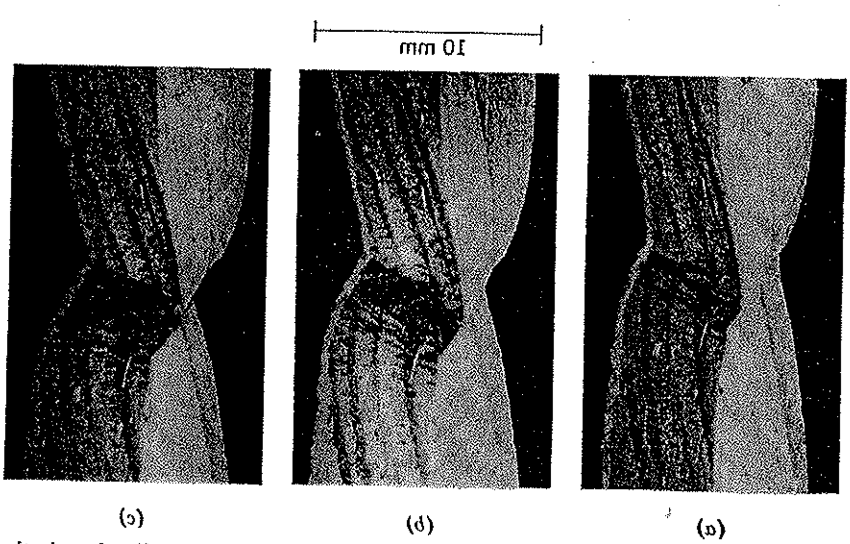

Fig. 5. Development of a ductile fracture by shear along a secondary slip plane in the neck of an aluminum crystal. Three stages.

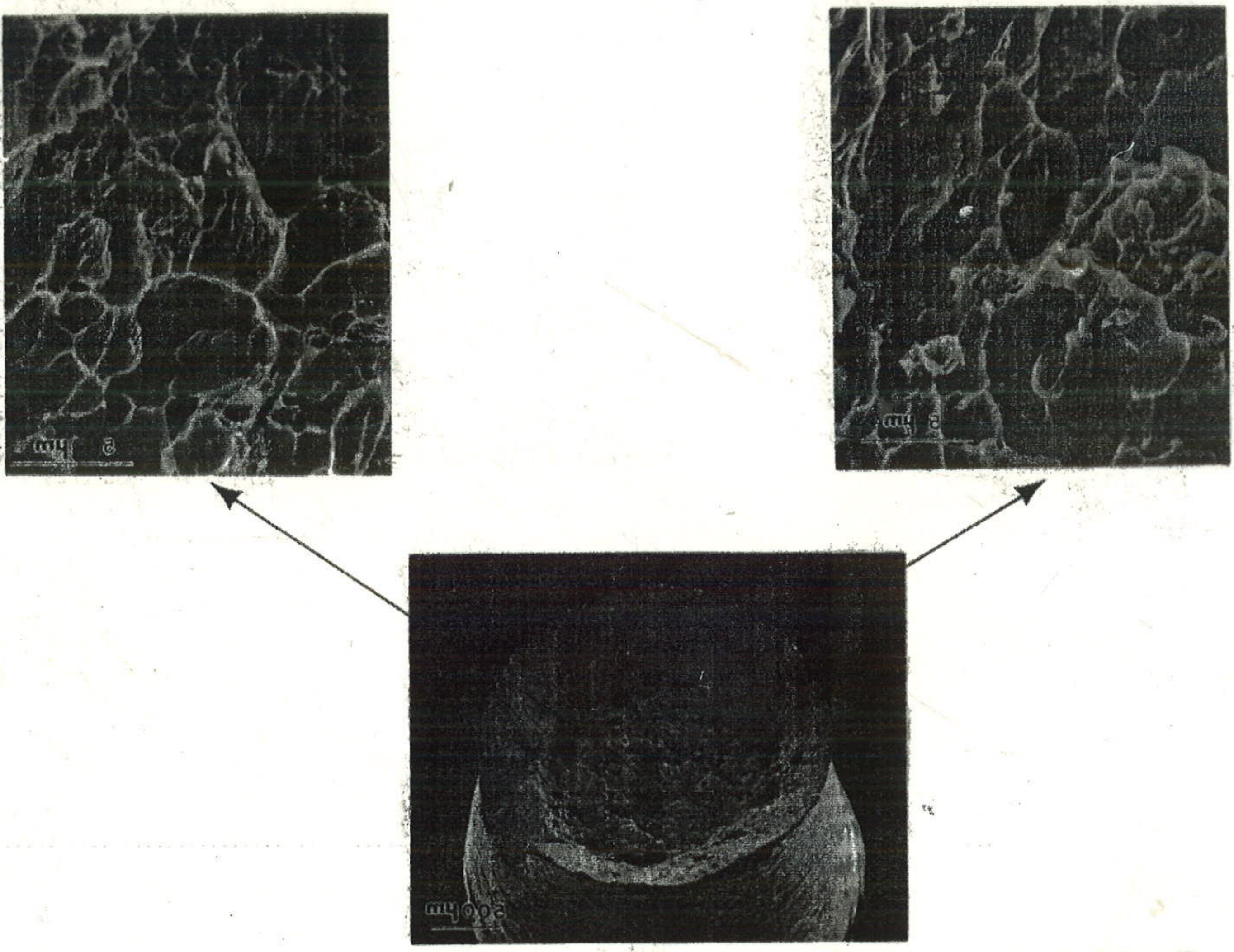

Figure 8.13 Scanning electron micrographs at low magnification (center) and high magnification (right and left) of AISI 1008 steel specimen ruptured in tension. Notice the equiaxal dimples in the central region and elongated dimples on the shear walls (the sides of the cup).

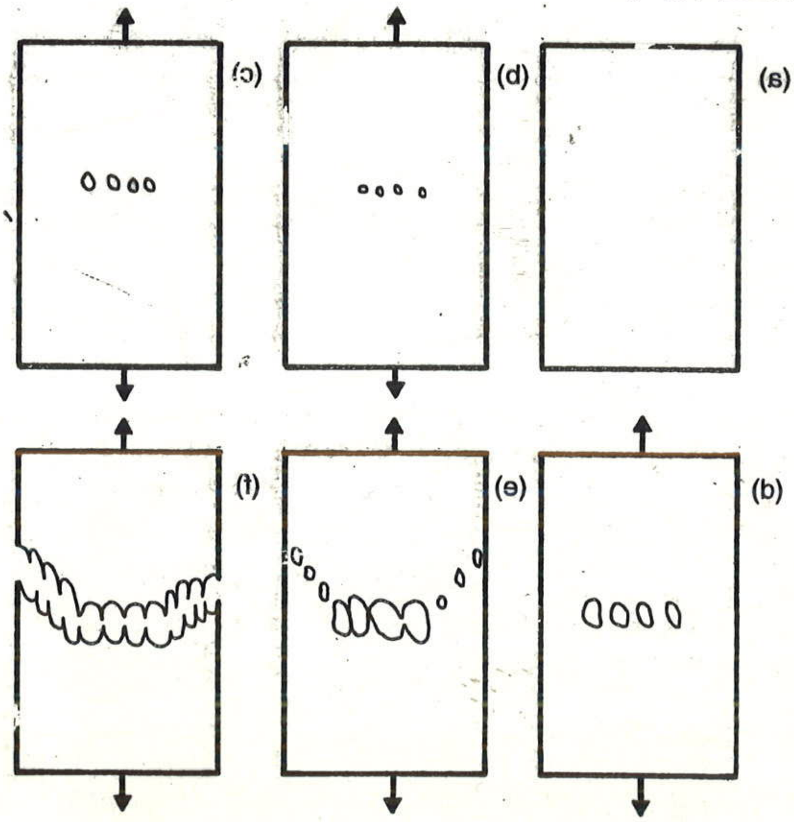

Figure 8.14 Schematic sequence of events leading to the formation of a cup-and-cone fracture.

TABLE 8.2 Compressive, Tensile, and Flexural Strengths of Ceramics (Adapted with permission from *Guide to Engineered Materials* (Metals Park, OH: ASM International, 1985), p. 16)

		Compressive Strength, MPa	*Tensile Strength, MPa*	*Flexural Strength, MPa*
Alumina	85	1,620	120	290
(different	90	2,415	140	320
purities)		2,067	170	310
	95	2,411	190	340
	99	2,583	210	340
Alumina silicate		275	17	62
ZrO_2–Al_2O_3		2,411		
3% 1/2 03 PSZ*		2,962		1,170
Transformation Toughened Zirconia		1,757	350	630
9% MgO Partially Stabilized Zirconia*		1,860		690
Cast Si_3N_4		138	24	69
Reaction-bonded SiC		689	140	255
Pressureless sintered SiC		3,858	170	550
Sintered SiC with free silicon		1,030	165	320
Sintered SiC with graphite		410	35	55
Reaction-bonded Si_3N_4		770		210
Hot-pressed Si_3N_4		3,445		860

*Data are from a variety of commercial sources.

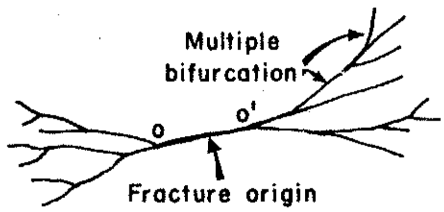

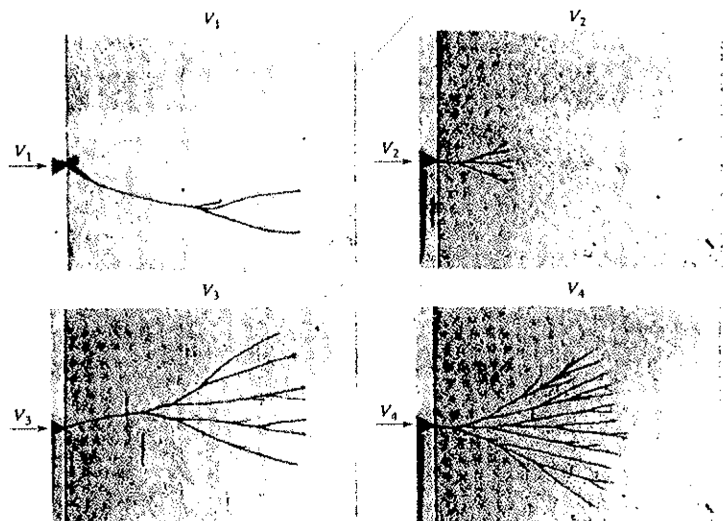

Figure 8.28 (a) Schematic illustrating a typical crack morphology in the vicinity of the origin, and (b) crack bifurcation in glass from an edge initiated failure, caused by sharp instrument blow on left-hand side; blow velocity $V_1 < V_2 < V_3 < V_4$. (Adapted from H. Schardin, in "Fracture," eds. B. L. Averbach, D. K. Felbeck, G. T. Hahn, and D. A. Thomas, MIT Press, Cambridge, Mass., 1959, p. 297, Chapter 16).

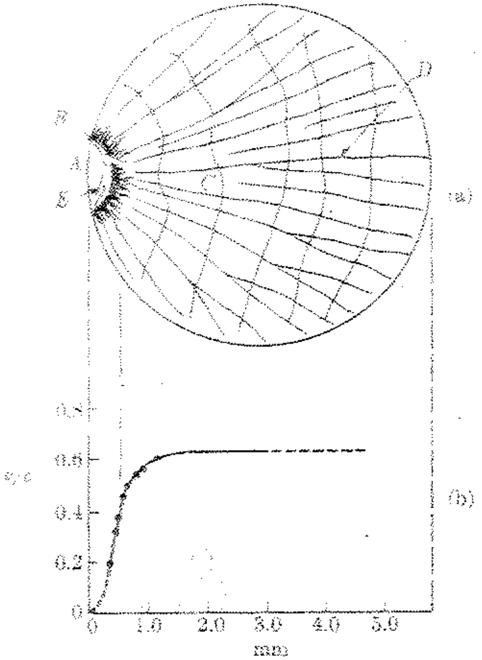

Fig. 15.10. (a) Schematic drawing of the appearance of the fracture surface of a rod (6-mm diameter) broken in bending. (b) Velocity of the crack at various points of the fracture. (After Smekal, 1952.)

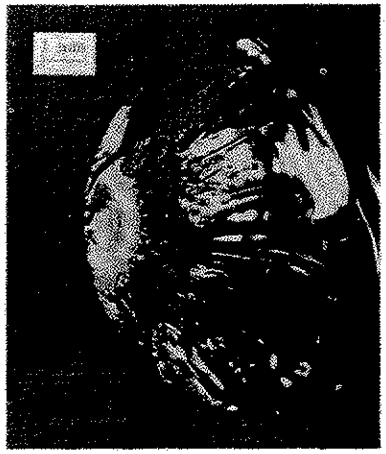

Fig. 15.11. Origin of fracture in a rod. Note Wallner lines in the fracture mirror.

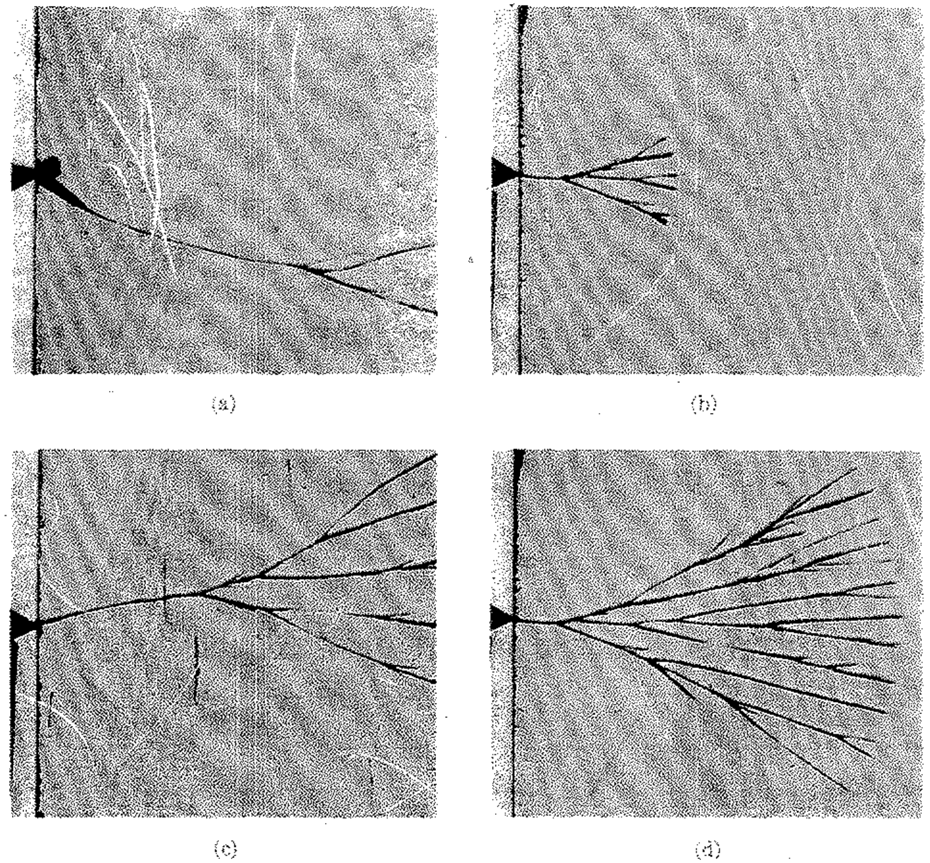

Fig. 15.9. Fracture in glass plate produced by striking knife edge at left; load increases from (a) to (d). (Schardin, 1959. Courtesy of M.I.T. Press.)

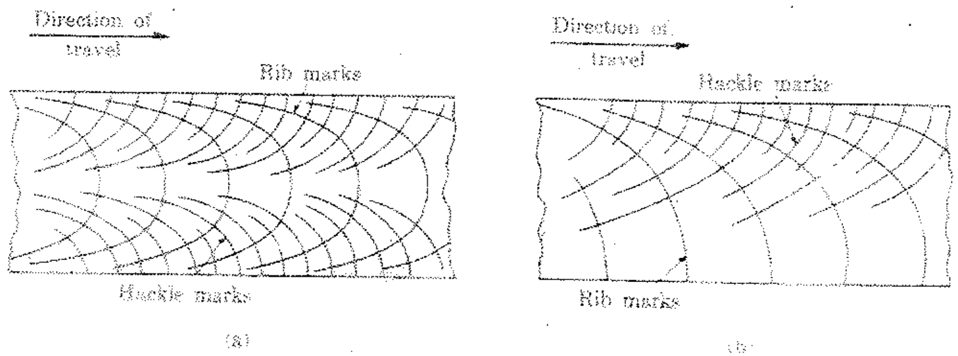

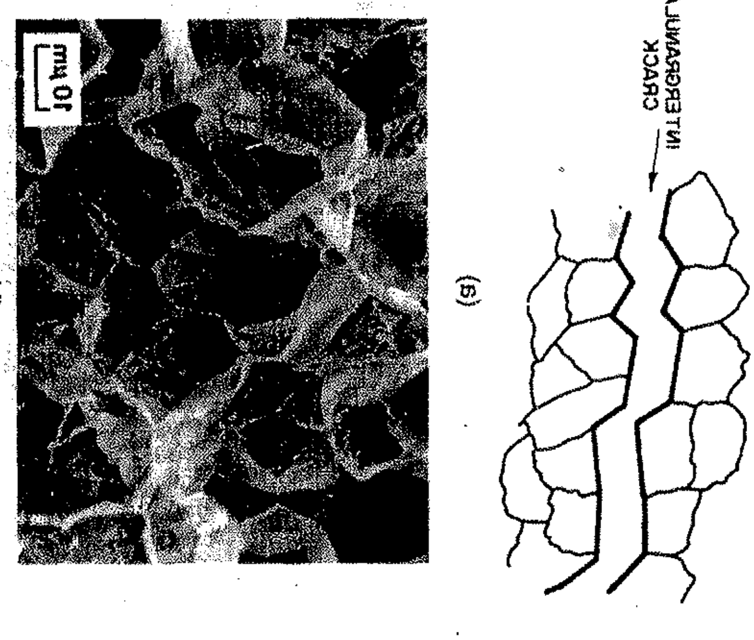

Figure 8.24 (a) An intergranular fracture (schematic). (b) Intergranular fracture in steel (scanning electron micrograph).

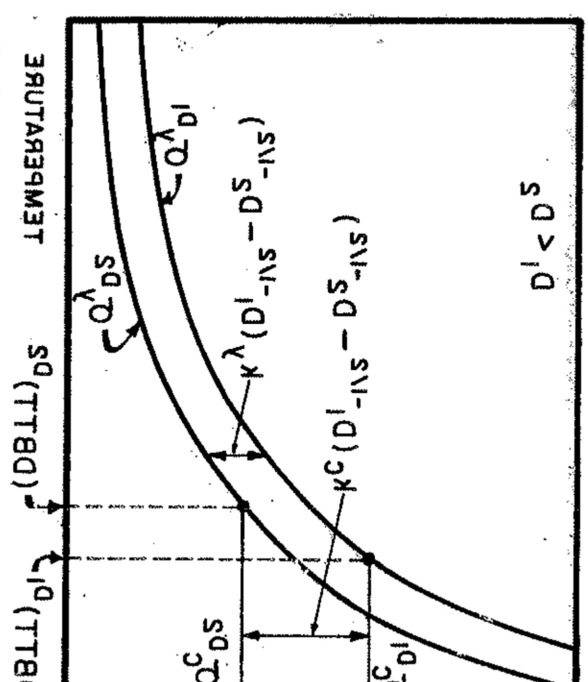

Figure 8.25 Armstrong criterion showing effect of grain size on ductile-to-brittle transition temperature.

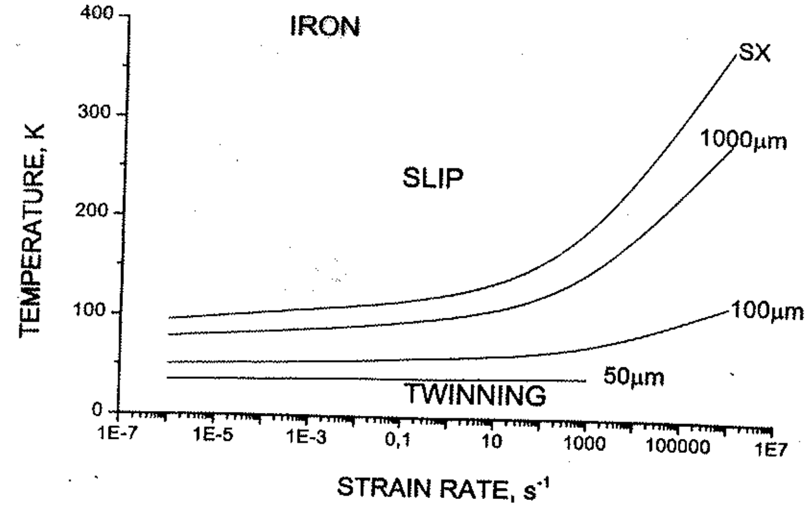

(a)

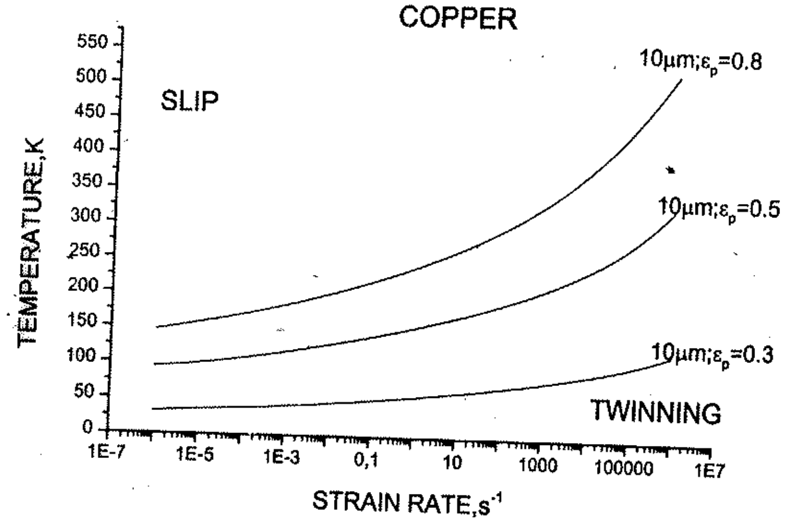

(b)

Fig. 8. (a) Calculated slip–twinning transition for iron of different grain sizes. (b) Calculated slip–twinning transition for copper (d = 10 μm), at different plastic strain levels: 0.3, 0.5, 0.8.

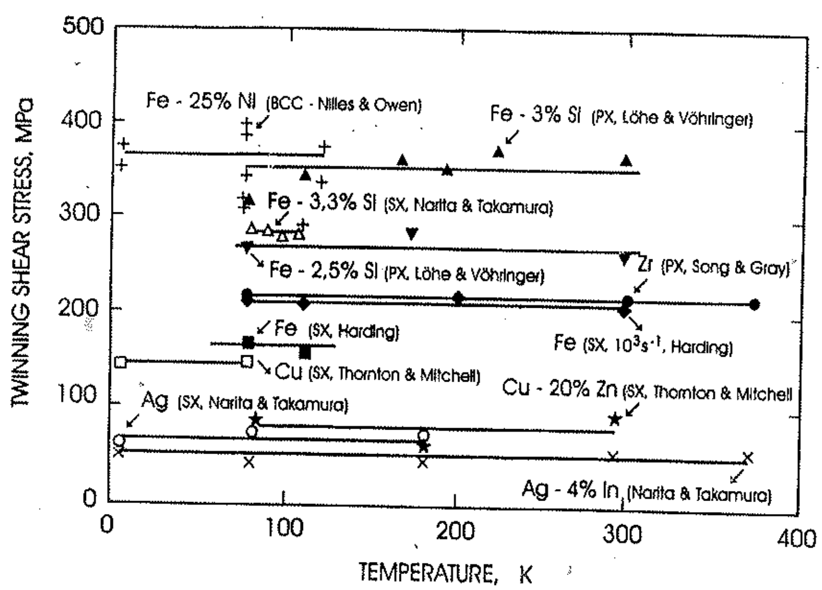

Fig. 6. Twinning stress as a function of temperature for a number of metals (both mono and polycrystals).

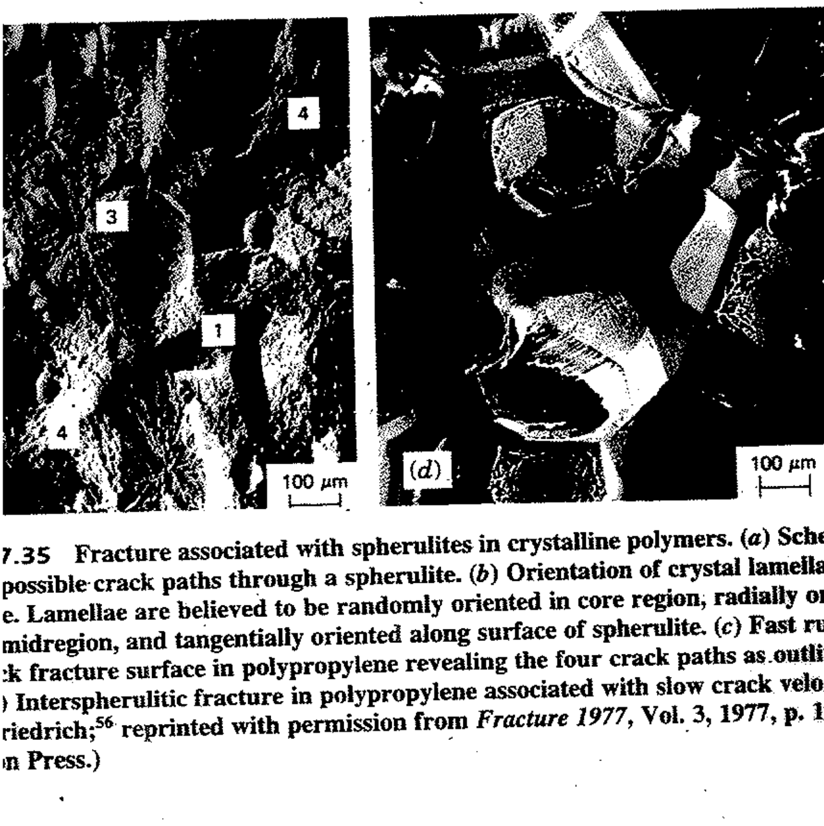

7.35 Fracture associated with spherulites in crystalline polymers. (*a*) Schema possible crack paths through a spherulite. (*b*) Orientation of crystal lamellae in e. Lamellae are believed to be randomly oriented in core region, radially ori- midregion, and tangentially oriented along surface of spherulite. (*c*) Fast run- k fracture surface in polypropylene revealing the four crack paths as outlined) Interspherulitic fracture in polypropylene associated with slow crack velocity. riedrich;[56] reprinted with permission from *Fracture 1977*, Vol. 3, 1977, p. 1119, n Press.)

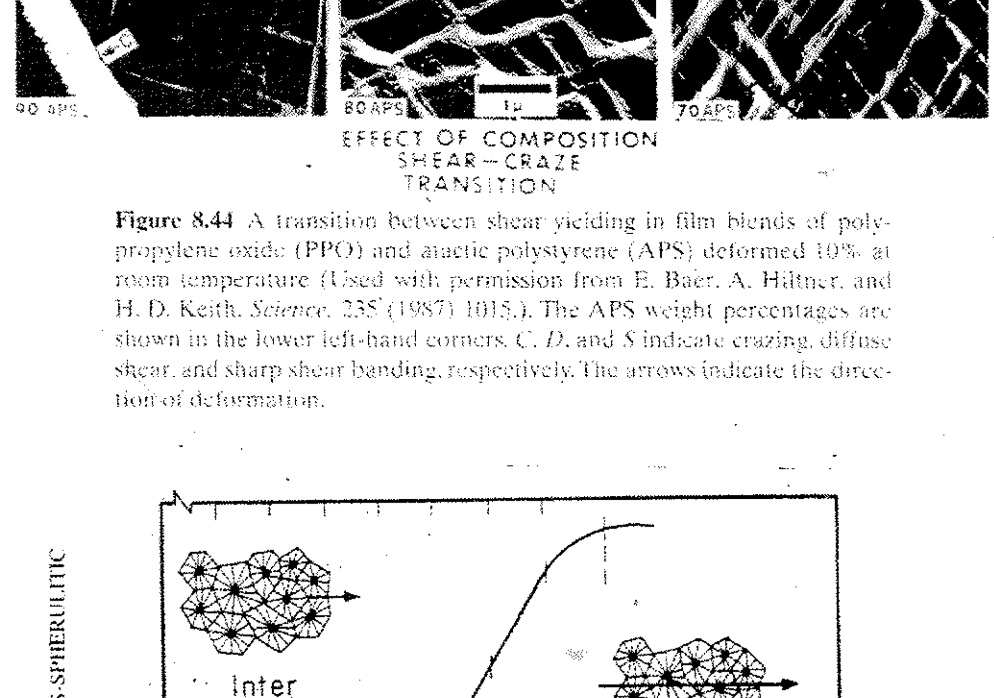

Figure 8.44 A transition between shear yielding in film blends of polypropylene oxide (PPO) and atactic polystyrene (APS) deformed 10% at room temperature (Used with permission from E. Baer, A. Hiltner, and H. D. Keith, *Science*, 235 (1987) 1015.). The APS weight percentages are shown in the lower left-hand corners. *C*, *D*, and *S* indicate crazing, diffuse shear, and sharp shear banding, respectively. The arrows indicate the direction of deformation.

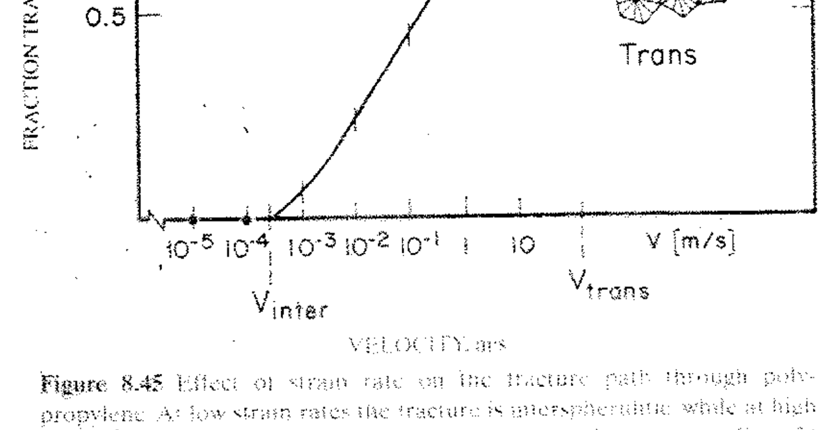

Figure 8.45 Effect of strain rate on the fracture path through polypropylene. At low strain rates the fracture is interspherulitic while at high strain rates it is transspherulitic (after J. M. Schultz, *Polym. Sci. & Eng.*, 24

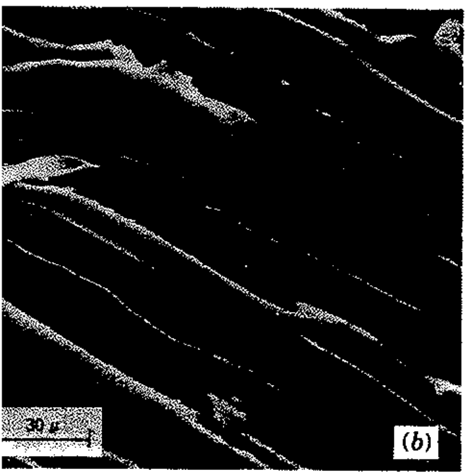

: along alternate craze–matrix inter-
:easing patch size in crack propagation
niversity.) (*b*) Stereoscan micrograph
'e the craze has been stripped off.
appear darker in this photograph.
Wiley & Sons, Inc.)

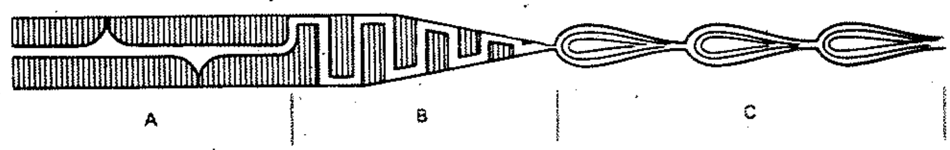

FIGURE 7.30 Model of crack advance in association with craze matter. Region A: crack advance by void formation through craze midplane. Region B: crack advance along alternate craze–matrix interfaces to form patch or mackerel patterns. Region C: crack advance through craze bundles to form hackle bands. (Adopted from Hull.[48])

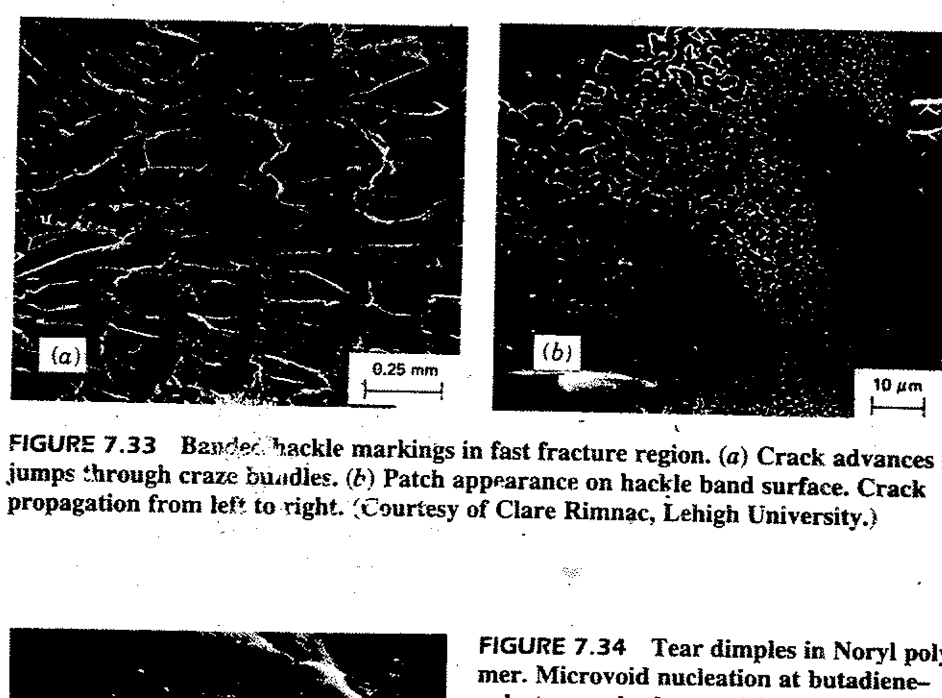

FIGURE 7.33 Banded hackle markings in fast fracture region. (*a*) Crack advances in jumps through craze bundles. (*b*) Patch appearance on hackle band surface. Crack propagation from left to right. (Courtesy of Clare Rimnac, Lehigh University.)

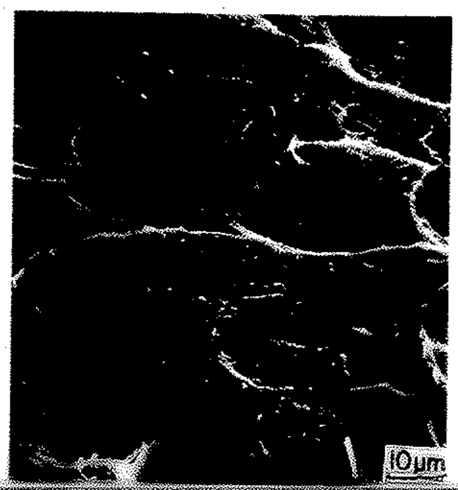

FIGURE 7.34 Tear dimples in Noryl polymer. Microvoid nucleation at butadiene–polystyrene duplex particles. (Courtesy of Clare Rimnac, Lehigh University.)